A Subgrid-Scale Deconvolution Approach for Shock Capturing

N. A. Adams[1] and S. Stolz

Institute of Fluid Dynamics, ETH Zürich, Switzerland
E-mail: adams@ifd.mavt.ethz.ch

We develop a method for the modeling of flow discontinuities which can arise as weak solutions of inviscid conservation laws. Due to its similarity with recently proposed approximate deconvolution models for large-eddy simulation, the method potentially allows for a unified treatment of flow discontinuities and turbulent subgrid scales. A filtering approach is employed since for the filtered evolution equations the solution is smooth and can be solved for by standard central finite-difference schemes without special consideration of discontinuities. A sufficiently accurate representation of the filtered nonlinear combination of discontinuous solution components which arise from the convection term can be obtained by a regularized deconvolution applied to the filtered solution. For stable integration the evolution equations are supplemented by a relaxation regularization based on a secondary filter operation and a relaxation parameter. An estimate for the relaxation parameter is provided. The method is related to the spectral vanishing-viscosity method and the regularized Chapman–Enskog expansion method for conservation laws. We detail the approach and demonstrate its efficiency with the inviscid and viscous Burgers equations, the isothermal shock problem, and the one-dimensional Euler equations.   © 2002 Elsevier Science (USA)

Key Words: shock capturing; large-eddy simulation; deconvolution; subgrid-scale modeling; compressible flows.

1. INTRODUCTION

The development of large-eddy simulation (LES) dates back to Smagorinsky [43] and Deardorff [8], who exploited the formal analogy of the unclosed subgrid-scale (SGS) stresses in LES with the unclosed Reynolds stresses in the Reynolds-averaged Navier–Stokes

---

[1] Permanent address: Institute of Fluid Mechanics, Technical University of Dresden, Germany. E-mail: Nikolaus. Adams@ism.mw.tu-dresden.de.

equations (RANS). In one space dimension the generic Smagorinsky model reduces to the von Neumann–Richtmyer artificial viscosity [38, 43]. A more general account of nonlinear viscosities in LES is given by Smagorinsky [44]. Both SGS modeling and shock-capturing methods subsequently developed along different paths. Leonard [28] has introduced the filtering concept as a formal framework for LES, by which SGS models can be derived as approximations of the filtered nonlinear products of nonfiltered quantities. In subsequent years a rapid development led to more sophisticated SGS models, the most prominent being the dynamic model [13] and the structure-function model [35]. References [31, 34] provide recent reviews on standard SGS models. Given the exact expression for the term to model, SGS modeling was addressed mainly from physical reasoning based on simplified nonlinear interaction mechanisms [30]. At the same time, the development of shock-capturing schemes was dominated by advances in numerical analysis based on the theorem of Lax and Wendroff [26] and on the concept of the entropy solution [25].

In the filtering approach to LES nonresolved scales are removed by convolving the underlying nonlinear transport equation with a filter [28]. Mostly only spatial filtering is applied. As a consequence, correlations of nonfiltered quantities arise from the nonlinear terms and require closure. A closure would be trivial if the filtering operation could be exactly inverted. An inverse-filter operation, however, is necessarily ill-posed, which reflects the fact that information about nonresolved scales is required. It was found that predictions of turbulent SGS stresses by models of eddy-viscosity type do not correlate well with the exact subgrid-scale stresses, and deficiencies of standard SGS models for anisotropic flows were attributed to this fact. SGS models involving an approximate inversion of the filter operation were expected to cope with the deficiencies of the eddy-viscosity models. The first of such models were based on Taylor expansions in the expressions for the filtered product of the velocity components [28] and on the assumption of scale-similarity [5]. Domaradzki and Adams [9] have reviewed SGS modeling approaches which directly model the SGS field.

For a real-space top-hat filter with the mesh spacing as filter width, the discretized LES equations become equivalent with a finite-volume discretization of the underlying conservation law. Flux-reconstruction, i.e., approximation of cell-face flux values from the cell-averaged (filtered) solution, is a central element of higher-order finite-volume methods. Harten *et al*. [16] have proposed higher order reconstructions based on local polynomials. Restricting the unfiltered solution to the space of local polynomials of a certain degree, the top-hat filter operation is regularized and can be inverted. This method can be extended to other filter kernels.

For the stable computation of discontinuous solutions the discretization of conservation laws requires an entropy regularization. A well-established method is to apply nonlinear limiters with the flux reconstruction [53]. It is illustrative to compare entropy regularization with the regularizing effect of SGS models. Considering isotropic turbulence Jiménez and Moser [19, 20] conclude that an accurate modeling of the subgrid-scale grid-scale interaction may not necessarily have a significant effect on the resolved scales. It appears rather that the SGS model is needed to generate the proper global energy dissipation. This observation suggests that SGS modeling may be coped with at least partially by an approach similar to an entropy regularization.

Eyink [10] has shown that the reduced regularity of turbulent subgrid scales provides a mechanism for dissipation even at infinite Reynolds number. As a consequence one may ask whether exact (spectral) solutions of the truncated Euler equations in three space dimensions give physically meaningful vanishing-viscosity solutions. For these solutions

an energy-equipartition spectrum is observed [30]. Solutions employing a shock-capturing scheme by Porter *et al*. [36] and Sytine *et al*. [49] on the contrary show physically more sensible properties with decaying energy spectra.

The obvious connection between numerical discretization and subgrid-scale modeling led Boris *et al*. [6], among others, to propose a "no-model" modeling strategy, where the subgrid-scale contributions are modeled by nonlinear numerical diffusion. This approach in fact delivers good results for jets [15]. Recently, it has been dubbed MILES, for "monotonically integrated LES," and was investigated in more detail by Fureby and Grinstein [11] and Garnier *et al*. [12]. Although the chosen shock-capturing algorithms were different (Fureby and Grinstein use a flux-corrected transport scheme; Garnier *et al*. investigate different high-resolution schemes based on finite differences), as a general trend it appears that MILES approaches work reasonably well for free shear flows and forced homogeneous turbulence at higher Reynolds numbers whereas they do not perform so well in general for decaying turbulence or at lower Reynolds numbers. Also the quality of MILES remains to be assessed for wall-bounded turbulent flows.

Further development on subgrid-scale modeling can benefit from encompassing the existing knowledge about entropy regularizations for numerical discretizations of conservation laws. Presently, studies are performed along two approaches, the first starting with a non-linearly stable discretization and analyzing the effective SGS model. Margolin and Rider [33] derive the SGS model implicitly given by their numerical scheme with the modified-differential equation method, which can also be employed to tune a numerical discretization such that a desired SGS model is represented implicitly [1]. The second approach is to modify SGS models such that they also can capture shocks. The dynamic model, for instance, does not have this property [2].

In this paper we attempt to contribute to a bridging of physical and numerical subgrid-scale modeling by introducing a model which extracts as much information as possible on the resolved scales, i.e., scales which have passed through the filtering operation, from the represented scales and which also ensures sufficient numerical-entropy dissipation. The former is achieved by a deconvolution operation on the represented scales, and the latter by a relaxation term employing a secondary filter operation on the represented nonresolved scales. We point out that given an exact deconvolution, the regularization when viewed in Fourier dual space resembles the spectral viscosity regularization of Tadmor [52], whereas the primary filtering operation of the conservation law is then equivalent to a subsequent postprocessing filtering. The spectral vanishing-viscosity method was applied to subgrid-scale modeling with favorable results by Karamanos and Karniadakis [22]. The proposed relaxation regularization is, however, formulated in real space, and it constitutes a lower order perturbation of the underlying conservation law and leaves the equation type unchanged. This is a considerable advantage over higher-order regularizations since the well-posedness conditions for the underlying conservation law transfer to the regularized system [14]. Spectral viscosity and superviscosity regularizations and the relaxation regularization proposed here try to maintain nonlinear stability of the solution without necessarily removing spurious oscillations from the nonpostprocessed (spectral superviscosity) or deconvolved (relaxation regularization) solution. A similar objective is pursued by the streamline diffusion method, introduced by Hughes and Brooks [17], which can exhibit spurious oscillations near discontinuities [18].

In Section 2 we detail the convolution filtering of the underlying conservation law and define the filter kernels and their discrete representation. The subgrid-scale model is explained

and analyzed in Section 3. A brief summary of the numerical discretization of the filtered conservation law used for the computational examples is given in Section 4. In Section 5 we apply the subgrid-scale model to the inviscid and viscous Burgers equations on a periodic domain, to the isothermal one-dimensional Euler equations on a finite domain for slow shocks, and to the full one-dimensional Euler equations on a finite domain investigating shock interaction with an entropy wave and shock–shock interactions.

2. FILTERING APPROACH

For a given generic nonlinear transport equation

$$\frac{\partial u}{\partial t} + \frac{\partial F(u)}{\partial x} = 0, \quad 0 \le x \le L, \tag{1}$$

a filtered transport equation for the filtered variable $\bar{u}$,

$$\frac{\partial \bar{u}}{\partial t} + \frac{\partial F(\bar{u})}{\partial x} = \mathcal{G}, \tag{2}$$

is obtained by convolution with a homogeneous filter,

$$\bar{u}(x) = \int_{-\infty}^{+\infty} G(x - x')u(x')\, dx' = G * u, \tag{3}$$

where

$$\mathcal{G} = \frac{\partial F(\bar{u})}{\partial x} - G * \frac{\partial F(u)}{\partial x} \tag{4}$$

is an error term due to the filtering. Equation (2) is the modified differential equation for $\bar{u}$, the solution of which would be identical to the filtered solution of (1) if $\mathcal{G}$ could be computed exactly.

Numerical discretizations of (2) carry wavenumbers ξ up to the Nyquist wavenumber $\xi_N = \pi/h$, where $h = L/N$ is the uniform grid spacing and N is the number of intervals into which the domain $[0, L]$ is partitioned. We call ξ_N the *numerical cutoff wavenumber*. If $u_N = \mathcal{P}_N u$ is the projection of the solution u onto the grid $\{x_i\}_{i=1}^{N+1}$ we can write the discretization of Eq. (2) as

$$\frac{\partial \bar{u}_N}{\partial t} + \frac{\partial F_N(\bar{u}_N)}{\partial x} = \mathcal{G}_1 + \mathcal{G}_2, \tag{5}$$

where

$$\mathcal{G}_1 = \frac{\partial F_N(\bar{u}_N)}{\partial x} - G * \frac{\partial F_N(u_N)}{\partial x},$$
$$\mathcal{G}_2 = G * \frac{\partial F_N(u_N)}{\partial x} - G * \frac{\partial F_N(u)}{\partial x}. \tag{6}$$

For the low-pass filter operation (3) we discern between wavenumbers $0 \le |\xi| \le \xi_C$, which we consider to be *resolved*, and wavenumbers $\xi_C < |\xi| \le \xi_N$, which we consider to be *nonresolved*, and we call ξ_C the *filter cutoff wavenumber*. For low-pass filters other than the spectral cutoff filter the determination of ξ_C is a matter of definition. It is obvious that

the ratio ξ_C/ξ_N should be chosen such that ξ_C can be considered to be well resolved by the underlying numerical discretization scheme [46]. For finite-difference schemes the relevant error measure is given by the modified wavenumber concept [54].

If we assume that u_N can be recovered exactly from $\bar{u}_N$ at every time instant, then the discretization of Eq. (2) reduces to a discretization of Eq. (1) with a postprocessing filter G applied during the time integration. It is known that the solution of the discretized Eq. (2) in this case fails to converge to the correct entropy solution [50]. Accordingly, an additional regularization of Eq. (2) is required. Tadmor [51, 52] proposed spectral viscosity and spectral superviscosity regularizations, which require a spectral-space representation of the conservation law. Viscosity or superviscosity regularizations formulated in real space amount to adding higher order terms to the conservation law and, for nonperiodic finite domains, can require different boundary conditions for the modified form of Eq. (1) if the artificial viscosity does not vanish at the boundaries [7].

In this paper we propose a regularization in form of a relaxation term

$$\mathcal{R} = -\chi\,(\bar{u}_N - G_2 * \bar{u}_N),$$

where χ is the inverse of some relaxation-time parameter and G_2 is a secondary filter of convolution type (3). The equation which is solved numerically for $\bar{u}_N$ is then

$$\frac{\partial \bar{u}_N}{\partial t} + \frac{\partial F_N(\bar{u}_N)}{\partial x} = \mathcal{G}_1 + \mathcal{R}, \tag{7}$$

with a suitable approximation for $\mathcal{G}_1$.

2.1. Primary and Secondary Filter

For the primary-filter operation we choose as kernel the Gauß function. In real space the filter is defined as

$$G(x - x') = \sqrt{\frac{8}{\pi}} \frac{1}{\Delta} e^{-8\frac{(x-x')^2}{\Delta^2}}, \tag{8}$$

where Δ is the filter width. The Fourier transform of (8) is given by

$$\hat{G}(\xi) = e^{-(\frac{\Delta\xi}{4\sqrt{2}})^2}. \tag{9}$$

Given a constant grid spacing h, we set in the following the primary-filter width $\Delta = 4h$. As filter-cutoff wavenumber of the primary filter we set $\xi_C = \xi_N/2 = \pi/(2h)$ for which $\hat{G}(\xi_C) = 0.3$.

We require the discrete representations of the filter (8) to resemble closely the transfer function (9) of the analytic filter kernel. Unlike the continuous filter kernel its discrete representation is band limited to $|\xi| \le \xi_N$. The transfer functions of discretizations of (3) by standard quadrature formulas (e.g., trapezoidal rule of Simpson's rule) usually exhibit a considerable error, in particular at wavenumbers close to ξ_N. A convenient way for a more accurate numerical representation is to use a Padé filter [27, 37]. We define a filter to be of order m if the first nonvanishing derivative of its transfer function (its Fourier transform) is of order m at $\xi = 0$. Let **u** be an $(N + 1)$ vector containing the values of the grid function $u_i = u(x_i)$ obtained by sampling the solution $u(x)$ at a set of equally spaced nodes $x_j = x_0 + jh,\ 0 \le j \le N$. Let $\bar{\mathbf{u}}$ denote the vector of filtered values obtained by

applying the discrete filter $\mathbf{G}$ to $\mathbf{u}$, in matrix–vector notation $\bar{\mathbf{u}} = \mathbf{Gu}$. Here, we consider the special case in which $\mathbf{G} = \mathbf{M}_l^{-1}\mathbf{M}_r$, and $\mathbf{M}_l$, $\mathbf{M}_r$ are tridiagonal matrices. A one-parameter family of filters with $m = 2$ is given by

$$\alpha \bar{u}_{j-1} + \bar{u}_j + \alpha \bar{u}_{j+1} = a u_j + \frac{b}{2}(u_{j-1} + u_{j+1}), \tag{10}$$

where $a = (1/2 + \alpha)$ and $b = a$. For a finite domain various treatments are possible at the boundary points $j = 0$ and $j = N$. We in general impose no filtering at domain-boundary points. The kernel of a Gauß filter (8) with filter width $\Delta = 4h$ is well approximated in Fourier space if one chooses $\alpha = -0.2$ (Fig. 1b).

(a)

(b)
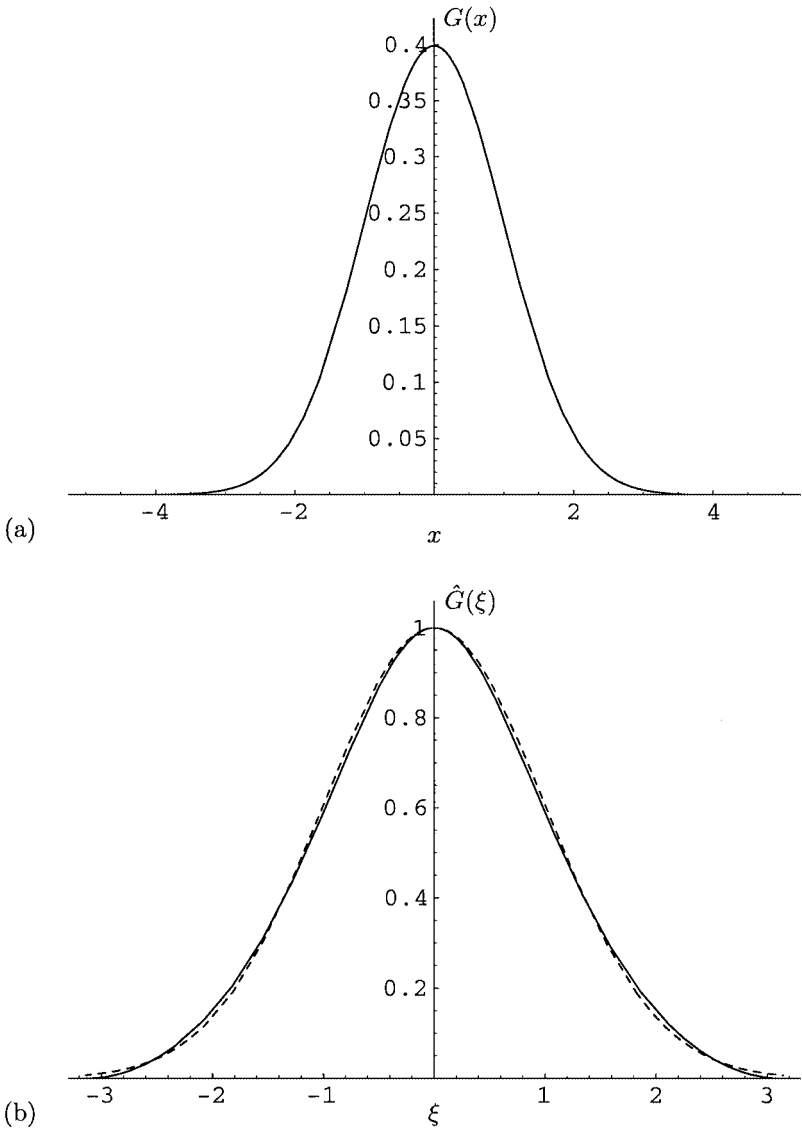
FIG. 1. Primary-filter kernel (8) with $\Delta = 4h$, $h = 1$. (a) Real space; (b) Fourier space. ——, Padé discretization; – – – –, exact.

For the secondary filter a second-order formulation and a twelfth-order formulation are investigated alternatively. For the secondary filter we use the notation $G_{2,p}$, indicating that the filter has order $2p$. The cutoff wavenumber ξ_{C_2} of the secondary filter should be larger than ξ_C.

(A) Second-order secondary filter.   By a relation given by Pruett and Adams [37] the parameter α of (10) can be linked to ξ_{C_2}. If the parameter is chosen as $\alpha = 0.49$ we obtain $\xi_{C_2} = 0.958\pi$ for $\hat{G}_{2,1}(\xi_{C_2}) = 0.3$. The transfer function of the filter kernel is shown in Fig. 2a.

(B) Twelfth-order secondary filter.   A $2p$-order secondary filter can be defined in Fourier space by taking the exponent of $\hat{G}$ to the pth power and using a secondary-filter

(a)

(b)
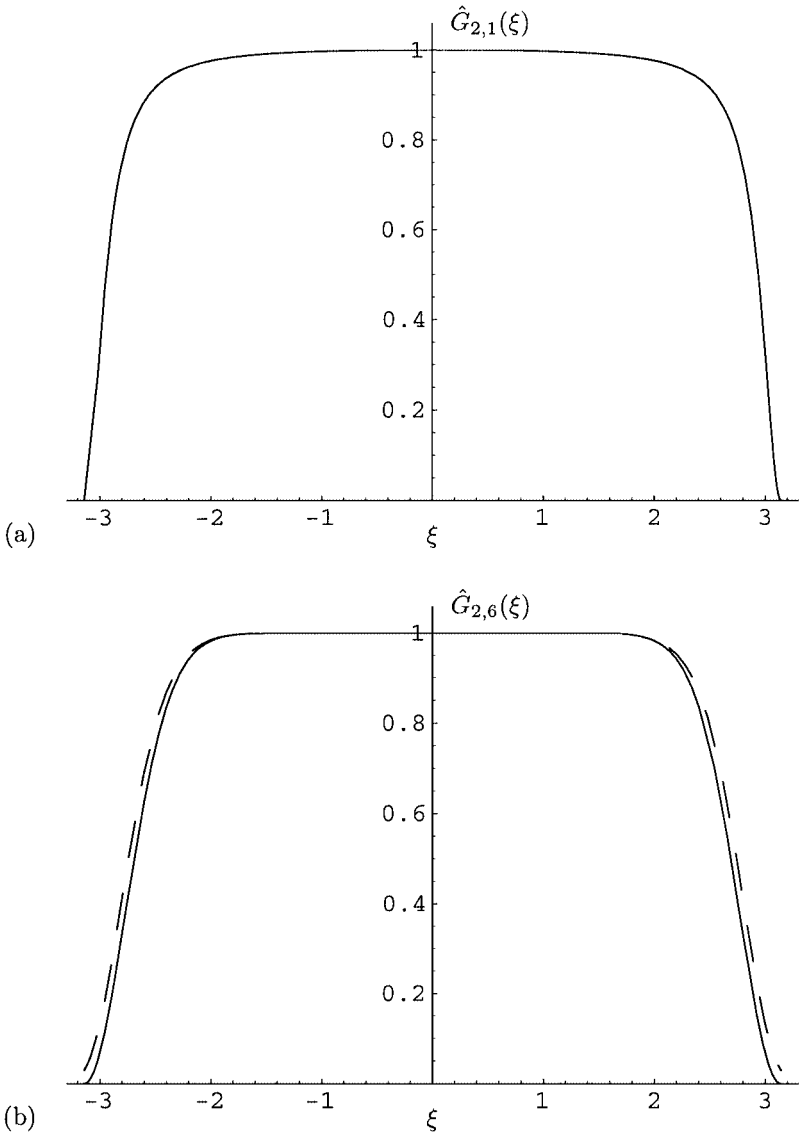
FIG. 2.   Transfer functions of the secondary-filter kernels. (a) Second-order filter (10) with $\alpha = 0.49$; (b) 12th-order filter. ———, Padé discretization; – – – –, exact.

width Δ_2:

$$\hat{G}_{2,p}(\xi) = e^{-(\frac{\Delta_2 \xi}{4\sqrt{2}})^{2p}}. \tag{11}$$

The real-space filter kernel can be obtained from the inverse Fourier transform

$$G_{2,p}(x) = \mathcal{F}^{-1}(\hat{G}_{2,p}). \tag{12}$$

For a secondary filter (11) with $\Delta_2 = 2h$ and $p = 6$ the exact transfer function $\hat{G}_{2,6}(\xi)$ is well approximated if one chooses $\alpha = 0.2$ in (10) and defines the discrete representation of $\hat{G}_{2,6}$ by

$$\mathbf{G}_{2,6} = \mathbf{M}_l^{-1}\mathbf{M}_r \sum_{\nu=0}^{5} \left(\mathbf{I} - \mathbf{M}_l^{-1}\mathbf{M}_r\right)^{\nu} = \mathbf{G} \sum_{\nu=0}^{5} (\mathbf{I} - \mathbf{G})^{\nu}, \tag{13}$$

where $\mathbf{I}$ is the unit matrix [45]. The cutoff wavenumber is $\xi_{C_2} = 0.898\pi$ for $\hat{G}_{2,6}(\xi_{C_2}) = 0.3$. A comparison of the transfer functions of the 12th order filters (12) and (13) is shown in Fig. 2b. More generally, a $2p$-order filter $G_{2,p}$ can be constructed from a second-order filter by

$$G_{2,p} = G * \sum_{\nu=0}^{p-1} (I - G)^{\nu},$$

where I is the identity operator $u = I * u = \int \delta(x - x')u(x') \, dx'$.

In the following we use G and $G_{2,p}$ synonymously for the discrete approximations of the corresponding continuous filter kernels G and $G_{2,p}$, respectively. Note that the discrete filter kernels are band-limited functions and thus have continuous real-space representations using Whittaker's cardinal function [54].

3. SUBGRID-SCALE MODELING

Subgrid-scale modeling consists of two parts: (i) approximation of the error term $\mathcal{G}_1$ in Eq. (7), and (ii) construction of an appropriate regularization $\mathcal{R}$ in Eq. (7) which is a model of $\mathcal{G}_2$ in Eq. (5). $\mathcal{G}_1$ can be computed exactly if the primary-filter operation with the kernel G is invertible on the restriction of its domain to all band-limited functions $u_N(x)$ with wavenumbers $|\xi| \leq \xi_N$ or to grid functions with grid spacing $h = \pi/\xi_N$.

3.1. Approximate Deconvolution

Since $\hat{G}(\xi)$ has compact support it is not invertible in general. If we, however, restrict the domain of $\bar{u}_N = G * u_N$ to band-limited functions or grid functions with wavenumbers $|\xi| \leq \xi_N$ then an inverse exists, provided $\hat{G}(\xi) > 0$ on $|\xi| \leq \xi_N$. The transfer function of the primary filter kernel defined in Section 2.1 vanishes at $|\xi| = \xi_N$ and a regularized inverse can be constructed on unbounded domains by a singular-value decomposition where the vanishing eigenvalue is removed. The approximate inverse of G is defined in Fourier dual space as

$$\hat{Q} = \begin{cases} \hat{G}^{-1}(\xi), & |\xi| < \xi_N, \\ 0, & |\xi| = \xi_N. \end{cases} \tag{14}$$

On bounded periodic domains the discrete filter operator G is a circulant matrix which is positive for N being odd. G has a zero eigenvalue for even N, and in this case the
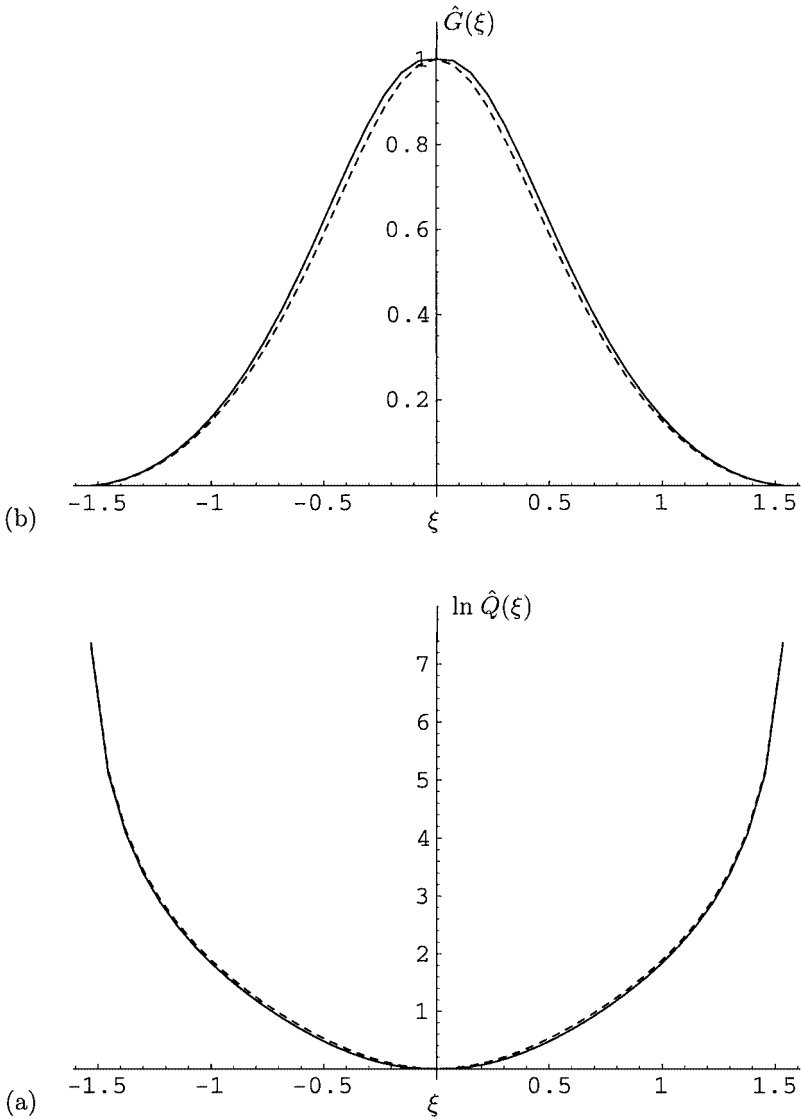
FIG. 3. Spectra of the discrete primary-filter kernels with $N = 40$. (a) Filter (10) with $\alpha = -0.2$; (b) inverse. ——, Nonperiodic domain; ----, periodic domain.

regularization (14) needs to be applied explicitly. On bounded nonperiodic domains an inverse of the discrete filter G exists if no filtering is imposed at the boundaries. In this case the spectrum of G is bounded away from zero on the positive real axis. In both cases, for symmetric filters the eigenvalues are real. In Fig. 3 we compare the spectra of the discrete primary filter and the spectra of the regularized inverse on a periodic and a nonperiodic domain, respectively.

Given a regularized inverse of the filtering operation, the term $\mathcal{G}_1$ in Eq. (5) can be approximated by replacing the unfiltered quantities in $F_N(u_N)$ with $\tilde{u}_N = Q * \bar{u}_N$, i.e.

$$\mathcal{G}_1 = \frac{\partial F_N(\bar{u}_N)}{\partial x} - G * \frac{\partial F_N(\tilde{u}_N)}{\partial x} = 0. \tag{15}$$

For now ignoring the contribution of $\mathcal{G}_2$ the following evolution equation applies for $\bar{u}_N$:

$$\frac{\partial \bar{u}_N}{\partial t} + G * \frac{\partial F_N(\tilde{u}_N)}{\partial x} = 0. \tag{16}$$

If the inversion is exact $Q * G = I$ we can write Eq. (16) also as

$$G * \left(\frac{\partial u_N}{\partial t} + \frac{\partial F_N(u_N)}{\partial x} \right) = 0. \tag{17}$$

It is known [50] that a solution u_N of this equation fails to satisfy the numerical-entropy condition for admissible discontinuous solutions. In order to introduce numerical-entropy dissipation Eq. (16) requires a regularization which models the effect of $\mathcal{G}_2$ in Eq. (5).

3.2. Relaxation Regularization

We construct a regularization based on a relaxation term which employs a secondary filter operation [47, 48]. The advantage of relaxation regularizations is that they leave the underlying differential equation type unchanged since they constitute a lower order perturbation and do not affect its well-posedness [14].

Regularization is achieved by adding a term

$$\mathcal{R} = -\chi(\bar{u}_N - G_{2,p} * \bar{u}_N), \tag{18}$$

where $\chi > 0$ is the inverse of some relaxation time and $G_{2,p}$ is a $2p$-order secondary filter of deconvolution type (3), to the right-hand side of Eq. (16). For $G_{2,p}$ either one of the secondary-filter kernels as defined in Section 2.1 can be used. The relaxation term has the following properties.

P1. The term is bounded:

$$\|I - G_{2,p}\|_2 \leq 1. \tag{19}$$

P2. The term vanishes asymptotically for a sufficiently smooth $\bar{u}_N$,

$$\lim_{\xi_N \to \infty} \|(I - G_{2,p}) * \bar{u}_N\|_2 = 0. \tag{20}$$

These properties ensure that Eq. (7) is consistent with Eq. (1). By condition (19) it is obvious that the relaxation term provides entropy dissipation for $\chi > 0$.

$$(\bar{u}, (I - G_{2,p}) * \bar{u}) = (\bar{u}, \bar{u}) - (\bar{u}, G_{2,p} * \bar{u}) \geq (\bar{u}, \bar{u})(1 - \|G_{2,p}\|_2) \geq 0 \tag{21}$$

using $\|G_{2,p}\|_2 \leq 1$, where $(\cdot, \cdot)$ is the inner product and $\| \cdot \|_2$ the corresponding 2-norm

$$\|u\|_2 = \left(\int |u|^2 \, dx \right)^{1/2}.$$

The amount of numerical-entropy dissipation is controlled by the choices for $G_{2,p}$ and for the relaxation parameter χ.

The relaxation term models the interaction between resolved and nonrepresented scales. We now derive an estimate for the relaxation parameter χ entering the subgrid-scale model. For this estimation we ignore the truncation errors introduced by the projection P_N and by the discrete approximation of the derivative operation ∂_x. Also, we neglect the deconvolution error so that the primary-filter operation can be bracketed out. For simplicity a periodic domain is used; for a nonperiodic domain boundary terms would enter the analysis. As a consequence of these simplifications, we consider the following regularized conservation law:

$$\frac{\partial u}{\partial t} + \frac{\partial F(u)}{\partial x} = -\chi (u - G_{2,p} * u). \tag{22}$$

We want to achive that the 2-norms of u and its first spatial derivative $\partial_x u$ can be bounded by the initial condition. The analysis resembles that of Schochet and Tadmor [41], who derived a similar result for a regularized Chapman–Enskog expansion (see also Section 3.3).

On multiplying Eq. (22) by u, integration over x, and applying Schwarz's inequality we obtain

$$\frac{1}{2}\partial_t \|u\|_2^2 = -\chi \|u\|_2^2 + \chi \int u G_{2,p} * u \, dx \leq \chi \|G_{2,p} * u\|_2 \|u\|_2 - \chi \|u\|_2^2. \tag{23}$$

The first expression on the right-hand side of relation (23) can be estimated by $\|G_{2,p} * u\|_2 \leq \|G_{2,p}\|_2 \|u\|_2$ and one obtains

$$\partial_t \|u\|_2 \leq -\chi \|u\|_2 (1 - \|G_{2,p}\|_2) \leq 0. \tag{24}$$

For the Fourier transform of the secondary-filter kernels it is $0 \leq \hat{G}(\xi) \leq 1$, so by the integral mean-value theorem $\|G_{2,p}\|_2 \leq 1$. We obtain the desired result that the 2-norm of the solution u of (22) is bounded by the initial condition

$$\|u\|_2 \leq \|u_0\|_2, \tag{25}$$

where $u_0 = u(x, 0)$.

Now we take the first derivative ∂_x of Eq. (22) giving

$$\underbrace{\partial_{tx} u}_{\text{I}} + \underbrace{\partial_{xx} F}_{\text{II}} = \underbrace{-\chi \partial_x u}_{\text{III}} + \underbrace{\chi G'_{2,p} * u}_{\text{IV}},$$

where $G'_{2,p} = \partial_x G_{2,p}(x - x')$. This equation is multiplied by $\partial_x u$. The contributions of the individual terms I through IV are

$$\int \partial_x u \, \partial_{tx} u \, dx = \frac{1}{2}\partial_t \|\partial_x u\|_2^2, \tag{26a}$$

$$\int \partial_x u \, \partial_{xx} F \, dx = \frac{1}{2} \int |\partial_x u|^2 \, \partial_x u \, F'' \, dx \tag{26b}$$

$$\int \partial_x u \, \partial_x u \, dx = \|\partial_x u\|_2^2, \tag{26c}$$

$$\int \partial_x u \, G'_{2,p} * u \, dx \leq \|\partial_x u\|_2 \|G'_{2,p} * u\|_2, \tag{26d}$$

where $F'' = \partial_{uu} F(u)$. Using these estimates we arrive after some manipulations at

$$\partial_t \|\partial_x u\|_2 + \chi \|\partial_x u\|_2 \left(1 - \frac{1}{\chi} \|\partial_x u\|_2 \|F''\|_2\right) \leq \chi \|G'_{2,p} * u\|_2$$

$$\leq \|G'_{2,p}\|_2 \|u\|_2.$$

For the secondary-filter kernels with $\int G_{2,p}(x)\,dx = 1$ the estimate

$$\|G'_{2,p}\|_2 \leq \xi_N$$

holds and one obtains

$$\partial_t \|\partial_x u\|_2 + \chi \|\partial_x u\|_2 \left(1 - \frac{1}{\chi} \|\partial_x u\|_2 \|F''\|_2\right) \leq \chi \xi_N \|u\|_2. \tag{27}$$

If we introduce the abbreviations

$$F''(u_0) = F_0'', \quad q(t) := \frac{1}{\chi} \|F_0''\|_2 \|\partial_x u\|_2,$$

$$Q := \frac{1}{\chi} \sup_t \|\partial_x u\|_2 \sup_t \|F_0''\|_2 \geq \sup_t q(t),$$

$$b = \xi_N \|u_0\|_2 \|F_0''\|_2,$$

Eq. (27) becomes

$$\partial_t q \leq -(1 - Q)\chi q + b.$$

Q is obviously positive and we now also assume that $Q < 1$, which always can be achieved by choosing χ large enough if $q(t)$ is bounded. On applying Gronwall's lemma the relation

$$q(t) \leq e^{-\chi(1-Q)t} q_0 + \frac{b}{\chi(1-Q)} \left(1 - e^{-\chi(1-Q)t}\right) \tag{28}$$

results. Relation (28) is satisfied if

$$\chi(1 - Q)Q \leq \chi q_0 (1 - Q) + b. \tag{29}$$

If we now investigate the equality of this relation, the requirement of positive roots results in a condition for the relaxation parameter χ as

$$\chi > \|F_0''\|_2 (\|\partial_x u_0\|_2 + 4\xi_N \|u_0\|_2). \tag{30}$$

This result also confirms our initial assumption $Q < 1$. If χ is chosen according to relation (30) then $q(t)$ is bounded and as a result the 2-norm of the first derivative in x of the solution u of Eq. (22) is bounded.

With $\xi_N = \pi/h$, relation (30) provides a model expression for χ as

$$\chi = C_0 + \frac{C_1}{h}, \tag{31}$$

where C_0 and C_1 are constants determined by the initial data. This expression is used in the application examples in Section 5. Under the assumptions made for this analysis the 2-norm boundedness of the solution u of Eq. (22) and its derivative holds if χ is chosen according to estimate (30). For discretized forms of Eq. (22) and nonperiodic domains these assumptions are generally not satisfied and 2-norm boundedness of u and $\partial_x u$ cannot be guaranteed. Also, in practice the estimate (30) yields a too large value for χ. For these reasons, the practical significance of Eq. (31) is that it gives an estimate for χ if appropriate constants C_0 and C_1 are chosen. The examples of Section 5 indicate that the results are not very sensitive to variations of χ.

3.3. Relation of the Relaxation Regularization with Other Regularizations

3.3.1. *Spectral Vanishing Viscosity*

Assuming that the inverse operation $Q * \bar{u}$ is exact we start from Eq. (17). Equality is satisfied if the argument of the primary-filter operation vanishes. After a Fourier transform Eq. (17) becomes

$$\partial_t \hat{u}_N + i\xi \hat{F}_N = -\chi(1 - \hat{G}_{2,p})\hat{u}_N. \tag{32}$$

Parameters of the spectral vanishing viscosity method can be estimated up to multiplicative constants and leave some freedom to choose a value for a particular application [32, 52]. If we compare Eq. (32) with Eq. (2.3) of Tadmor [52] we can identify

$$\frac{(1 - \hat{G}_{2,p})}{(i\xi)^{2p}}$$

as the spectral viscosity smoothing factor. Given a $2p$-order secondary filter, $(1 - \hat{G}_{2,p})$ has a convergent Taylor-series expansion at $\xi = 0$, with the leading-order term being $\mathcal{O}(\xi^{2p})$. For $p > 1$ the leading-order term in the series expansion of $(1 - \hat{G}_{2,p})$ corresponds to a $2p$-order derivative in real space, which is usually called superviscosity or hyperviscosity. Since $\hat{G}_{2,p}$ is smooth, the effective size of the inviscid spectrum as defined by Tadmor [52] is $m = 0$. Since this violates Tadmor's assumption $m \propto N^\theta$, where $0 < \theta < 1$, we cannot expect to recover spectral accuracy with Eq. (32). It can be seen, however, from Fig. 4 that the relation (2.4c) of Tadmor [52],

$$\xi^{2p}\left(1 - \left(\frac{m}{|\xi|}\right)^{\frac{2s-1}{\theta}}\right) \leq 1 - \hat{G}_{2,p}(\xi) \leq \xi^{2p},$$

which determines admissible lower and upper bounds for the spectral viscosity transfer functions, is approximately satisfied by the secondary filters of Section 2.1.

3.3.2. *Regularized Chapman–Enskog Expansion*

Rosenau [40] has pointed out that the Chapman–Enskog expansion of the Boltzmann equation truncated at the second-order term (Burnett equation) gives rise to a fourth-order diffusion which can render the corresponding initial-value problem unstable. It is interesting to note that a similar situation occurs in subgrid-scale modeling when expansion–deconvolution methods are used [28, 29]. Rosenau [40] has proposed a regularized Chapman–Enskog expansion which results in a spectral viscosity which remains bounded at
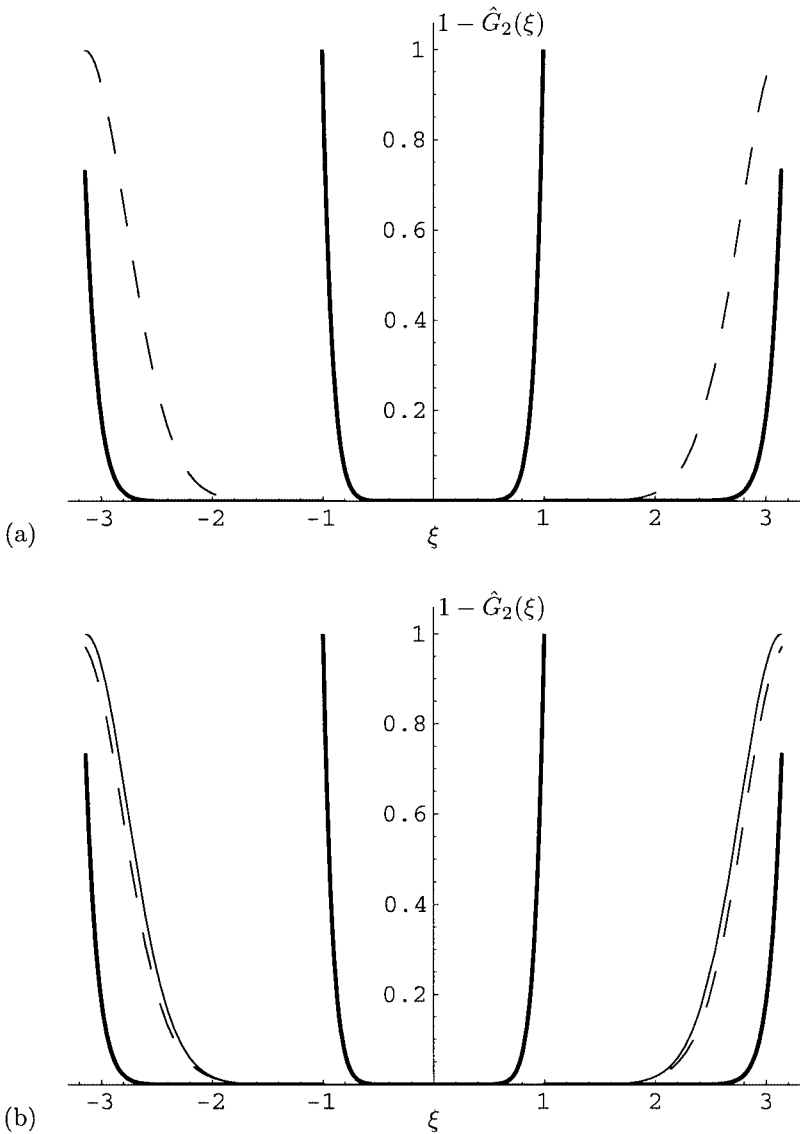
FIG. 4. (a) Second-order and (b) 12th-order secondary filter expressed as spectral superviscocity and compared with relation (2.4c) of Tadmor [52], where $N = 40$, $m = 1$, $h = 1$, $\theta = 0.3$, $s = 6$. ———, Analytic expression; ––––, discrete approximation; ——, lower and upper bound given by relation (2.4c) of Tadmor [52].

high wavenumbers. For a scalar equation (1) the Rosenau regularization would correspond to a relaxation regularization

$$\partial_t u + \partial_x F(u) = -\frac{\chi}{\Delta}(u - Q_\Delta * u),$$

$$Q_\Delta(x) = \frac{1}{2\Delta} e^{-|x|/\Delta},$$

as pointed out by Schochet and Tadmor [41].

3.3.3. *Finite-Element Interpretation*

Given the discrete filter Eq. (10), it can be readily shown that the semidiscrete equation for the initial value problem (22) can be written as

$$\alpha(\partial_t u(x_{j+1}, t) + \partial_t u(x_{j-1}, t)) + \partial_t u(x_j) + \alpha(\delta_x f(x_{j+1}, t) + \delta_x f(x_{j-1}, t)) + \delta_x f(x_j, t)$$
$$= -\chi\left(\frac{\alpha}{2}\Delta_+\Delta_- u(x_j, t) - \frac{1}{4}\Delta_+\Delta_- u(x_j, t)\right), \tag{33}$$

where δ_x stands for some discrete spatial-derivative operator, and Δ_+, Δ_- are the standard first-order forward and backward differentiation operators. In this respect the relaxation regularization can be interpreted as an artificial diffusion for a particular finite-element discretization of the underlying conservation law.

4. NUMERICAL DISCRETIZATION

For numerical discretization a sixth-order symmetric compact finite-difference scheme is used [27]. At interior mesh points the difference operator for a grid function $u_i = u(x_i)$ and its derivative $u_i' \doteq \partial_x u(x_i)$ is given by

$$u_{i-1}' + 3u_i' + u_{i+1}' = \frac{1}{h}\left(-\frac{1}{12}u_{i-2} - \frac{7}{3}u_{i-1} + \frac{7}{3}u_{i+1} + \frac{1}{12}u_{i+2}\right). \tag{34}$$

Toward nonperiodic boundaries the order of the scheme is dropped to 3. Boundary schemes as given by Lele [27] are used. We found that this scheme gives for all test cases better results than a second-order central finite-difference scheme. Time integration is performed with an explicit third-order Runge–Kutta scheme [55].
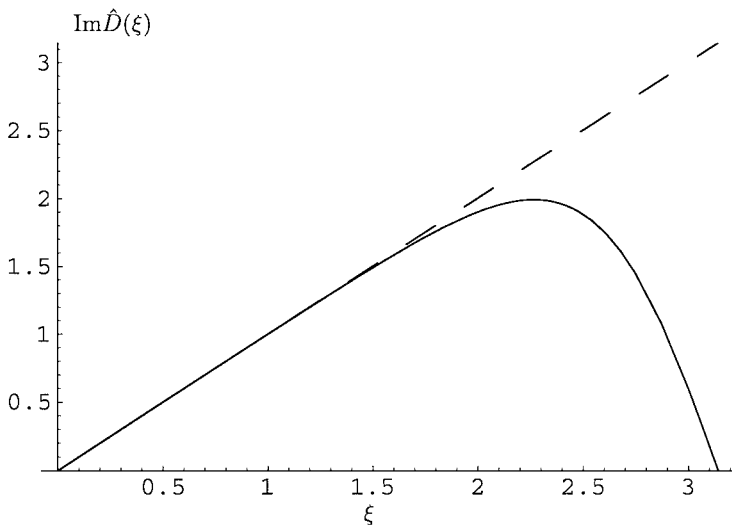

FIG. 5. Imaginary part of the transfer function $\hat{D}(\xi)$ for the first-derivative approximation by (34); the real part vanishes due to symmetry.

The spectral transfer function for (34) is shown in Fig. 5. Note that $\xi_C < \xi_R$, where wavenumbers $|\xi| \le \xi_R \simeq 2.2$ can be considered as well resolved by scheme (34).

The time-step size is determined by the following condition, which is monitored during the computation,

$$\tau = h\frac{\text{CFL}}{\max\limits_{x} \partial F/\partial u + h\chi}, \tag{35}$$

where for systems $\partial F/\partial u$ is replaced by the spectral radius of the Jacobian and CFL is a parameter. For large χ Eq. (22) can become stiff and a semiimplicit time integration would be more efficient than the explicit Runge–Kutta schemes used is Section 5. Due to
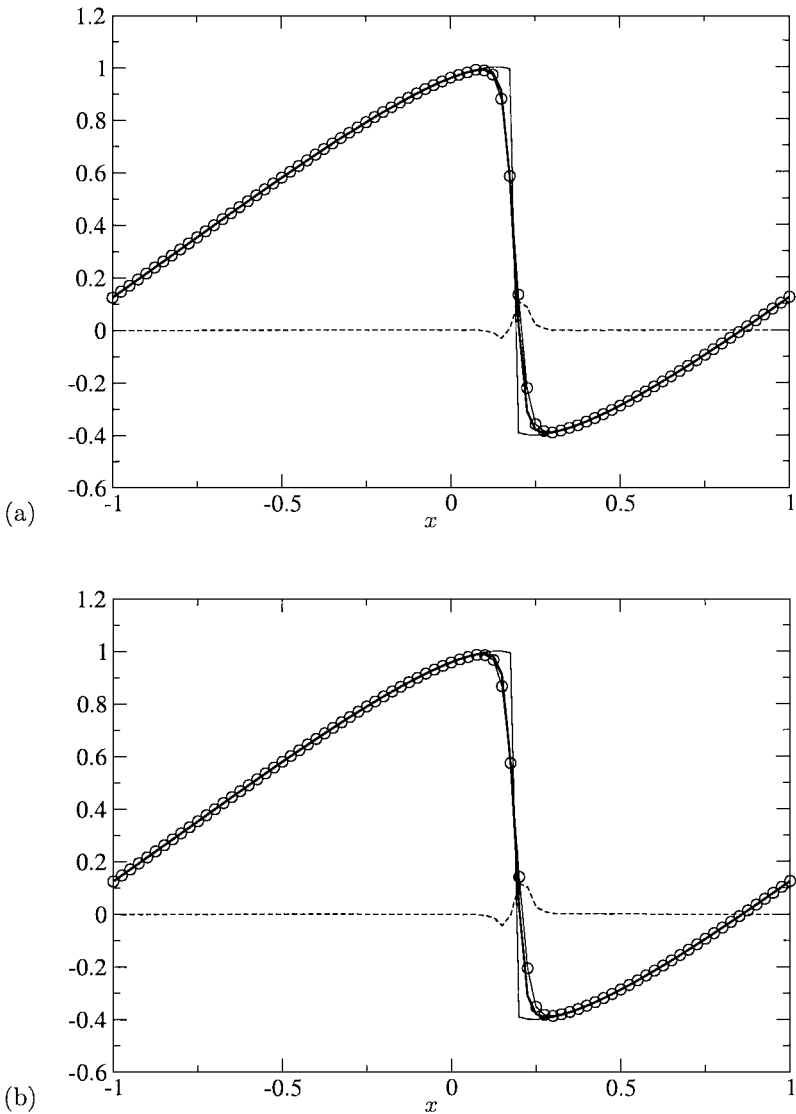
FIG. 6.   Solution for Burgers equation at $t = 2/\pi$, $N = 80$. (a) With second-order $G_{2,1}$; (b) with 12th-order $G_{2,6}$. ——, $\bar{u}_{exact}$; ——, u_{exact}; O–O–O, $\bar{u}$; - - - -, $(\bar{u}_{exact} - \bar{u})$.
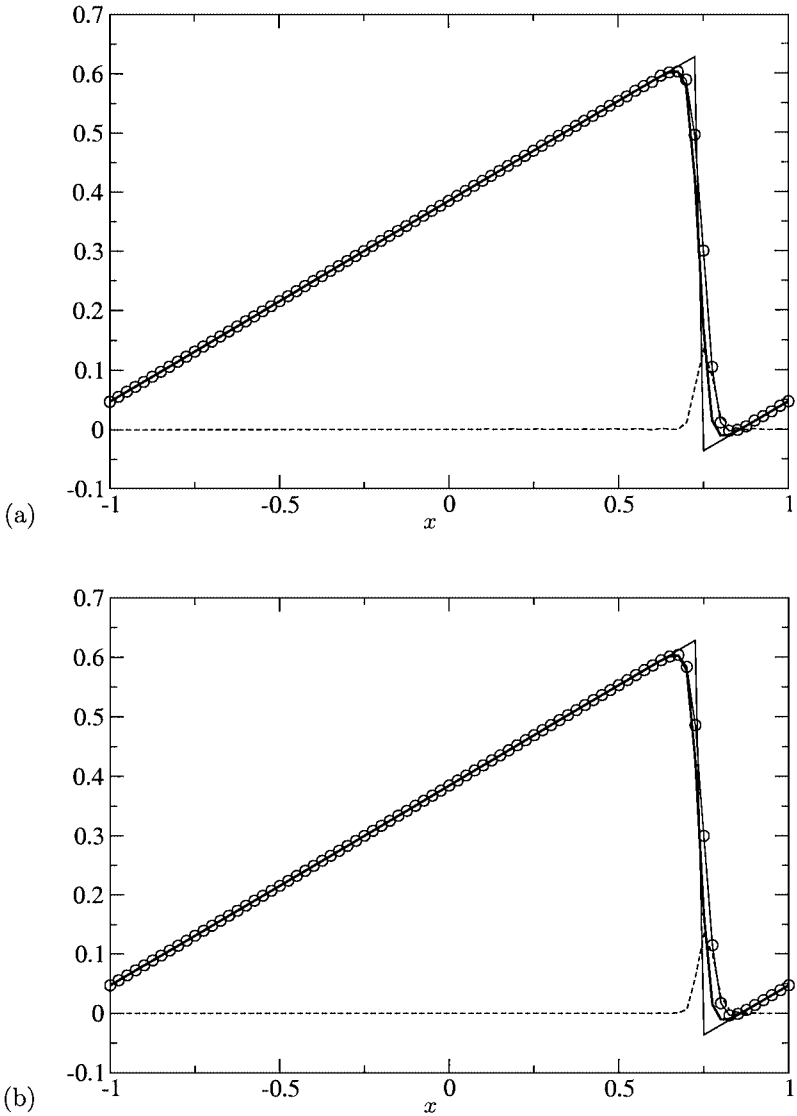
FIG. 7. Solution for Burgers equation at $t = 2.5$, $N = 80$. (a) With second-order $G_{2,1}$; (b) with 12th-order $G_{2,6}$. ———, $\bar{u}_{exact}$; ———, u_{exact}; O–O–O, $\bar{u}$; – – – –, $(\bar{u}_{exact} - \bar{u})$.

the linearity of the relaxation term a semiimplicit formulation, treating the relaxation term implicitly, does not significantly increase the computational effort.

We point out that the main rationale to use the high-order Padé scheme (34) is its good spectral-resolution capability. Since time integration is performed with a third-order scheme and h and τ are linearly related by (35) the consistency order of the fully discrete equation is $\mathcal{O}(h^3)$. The application of the present model to lower order schemes is the subject of a separate study.

5. RESULTS

In the following we call Eq. (7) with (15) and (18) the direct-deconvolution model (DDM). Two different formulations for the secondary-filter kernel $G_{2,p}$ are compared. The first is the
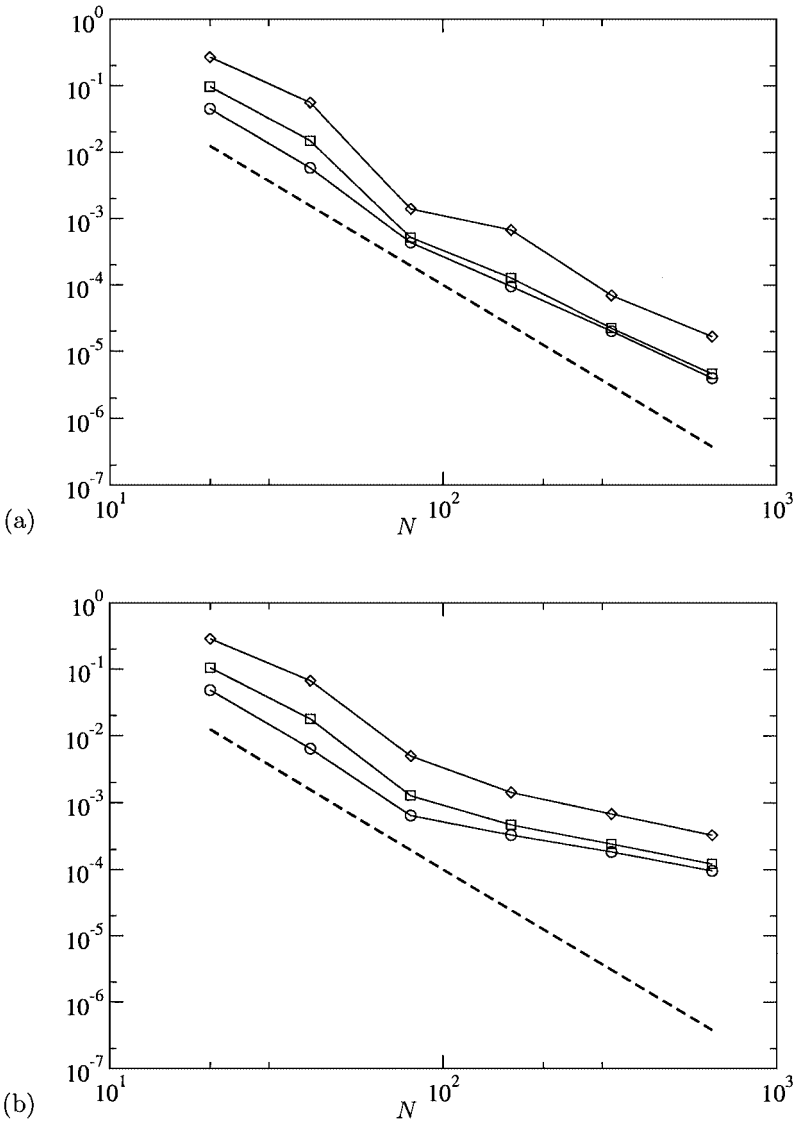
FIG. 8. Error norms for Burgers equation solution at $t = 2/\pi$. (a) With second-order $G_{2,1}$; (b) with 12th-order $G_{2,6}$. $\bigcirc\!\!-\!\!\bigcirc\!\!-\!\!\bigcirc$, L_1-error; $\square\!\!-\!\!\square\!\!-\!\!\square$, L_2-error; $\diamond\!\!-\!\!\diamond\!\!-\!\!\diamond$, L_∞-error; $----$, N^{-3}.

second-order formulation $G_{2,1}$, where the discrete filter is defined by Eq. (10) with $\alpha = 0.49$. The second is the 12th-order formulation $G_{2,6}$ according to Eq. (13), with $\alpha = 0.2$. We consider first an N-wave solution for the periodic inviscid Burgers equation, which constitutes the simplest example of a hyperbolic nonlinear conservation law. If the initial condition contains a range of scales and if a nonvanishing viscosity is considered, one obtains a one-dimensional model of turbulence suitable for assessing subgrid-scale models [4]. This case is investigated secondly. Third, we apply our approach to the isothermal Euler equations in one space dimension with the main objective being to assess its performance for the so-called "slow-shock problem" [39]. Fourth, we consider the blast-wave situation of Woodward and Colella [56], which constitutes a challenging test for shock-capturing schemes, involving
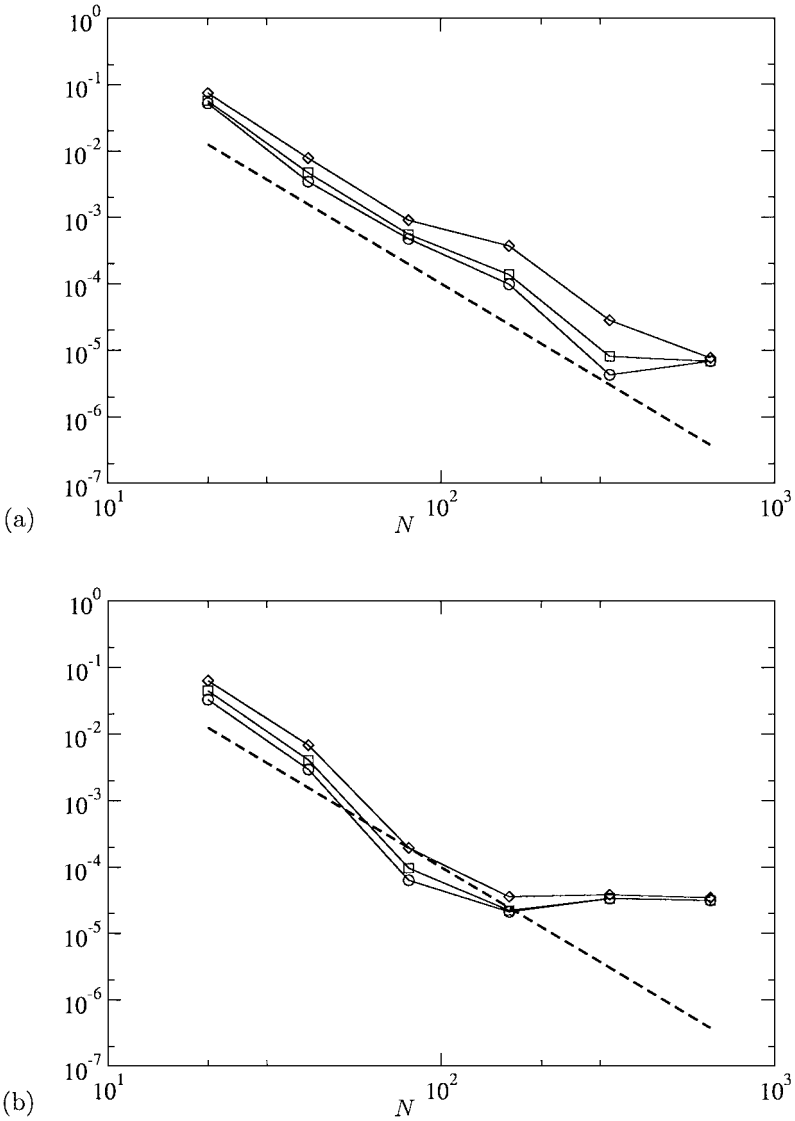
FIG. 9. Error norms for Burgers equation solution at $t = 2.5$. (a) With second-order $G_{2,p}$; (b) with 12th-order $G_{2,p}$. O–O–O, L_1-error; □–□–□, L_2-error; ◇–◇–◇, L_∞-error; $----$, N^{-3}.

wave reflections from solid boundaries. Fifth, we study the full Euler equations in one space dimension, where we are interested in the interaction of disturbances with a shock.

5.1. Inviscid Burgers Equation

The variable u of Eq. (1) is a scalar and the flux function is $F(u) = u^2/2$. The solution u is 2-periodic, and the initial condition is given by $u_0(x) = 0.3 - 0.7 \sin(\pi x)$, $-1 \le x < 1$. The time-step size τ is determined by Eq. (35) with CFL $= 0.5$. For the relaxation parameter we set the minimum value given by Eq. (30), which for the above initial condition is

$$\chi \simeq 2.2 + \frac{13}{h}.$$
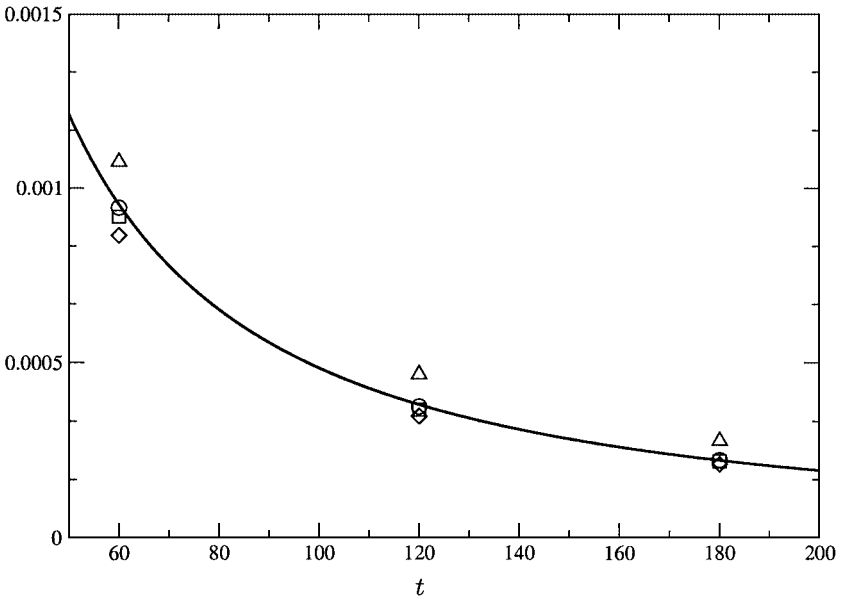
FIG. 10. Energy $E(t)$ at times $t = 60$, 120, and 160 compared with direct simulation (———). $\triangle$, $N = 256$; $\diamond$, $N = 512$; $\square$, $N = 1024$; $\bigcirc$, $N = 2048$.

Figure 6 shows the results obtained at time $t = 2/\pi$ with the second-order secondary filter (Fig. 6a) and with the 12-th order secondary filter (Fig. 6b) with $N = 80$ grid points. The agreement between the filtered exact solution $\bar{u}_{exact}$ and the numerical approximation $\bar{u}$ is good in both cases. The same holds for the results at the later time $t = 2.5$, as shown in Fig. 7.

The error norms for different resolutions $N = 20, 40, \ldots, 640$ each for the second-order and the 12th-order secondary-filter formulation are shown in Fig. 8 for the solutions at time
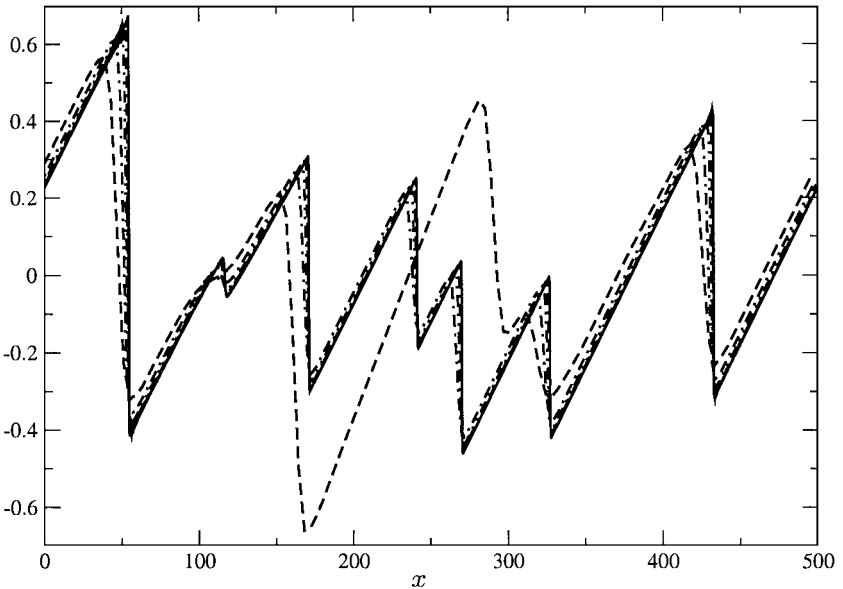
FIG. 11. Instantaneous solution $\bar{u}(x, t)$ compared with direct simulation $u(x, t)$ (———) at time $t = 180$. $----$, $N = 256$; $-\cdot-$, $N = 512$; $-\cdot\cdot-$, $N = 1024$; $\cdot--\cdot$, $N = 2048$.
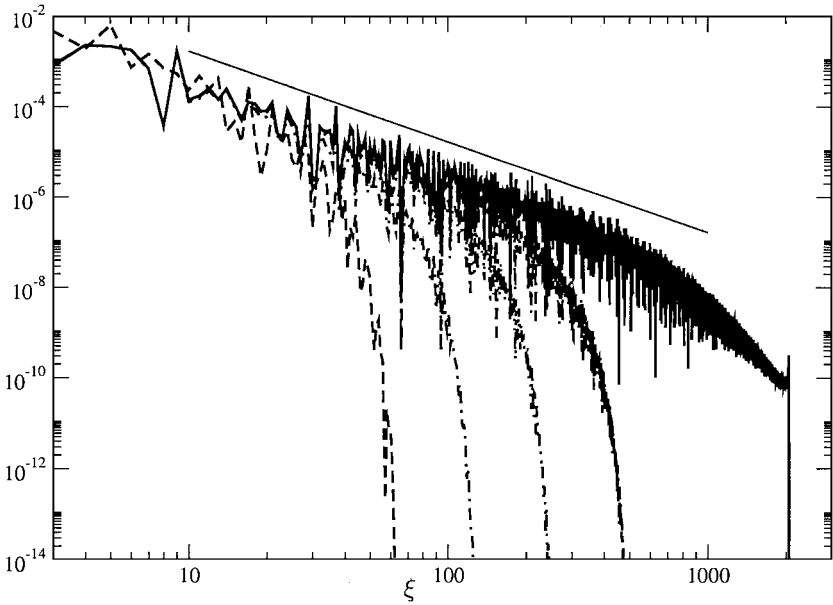
FIG. 12. Instantaneous spectra $|\hat{\bar{u}}(\xi)|^2$ compared with direct simulation $|\hat{u}(\xi)|^2$ (———) at time $t = 180$. – – – –, $N = 256$; –··–, $N = 512$; ——··——, $N = 1024$; –· –·, $N = 2048$; ———, ξ^{-2}.

$t = 2/\pi$, and at time $t = 2.5$ in Fig. 9. Both filter formulations exhibit roughly a third-order convergence rate, which corresponds to the truncation error of the time-integration scheme. For the higher order secondary filter we note, however, that round-off effects set in rather early and beyond about $N = 100$ the error-decay degrades.

5.2. One-Dimensional Burgers Turbulence

The variable u of Eq. (1) is a scalar and the flux function is $F(u) = u^2/2 + \nu \partial_x u$. The solution u is L-periodic. For consistency with the results of Aldama [4] we set $\nu = 0.02$, $L = 500$. The initial data are computed from a u distribution with initial spectrum

$$E_0(\xi) = \frac{1}{2}|\hat{u}_0(\xi)|^2 = A\xi'^4 e^{-\sigma^2 \xi'^2/2},$$

where $\xi' = 2\pi\xi/L$, $A = 10722.08$, $\sigma = 19.89$. The time-step size τ is determined by Eq. (35) with CFL $= 0.5$. We use the same relaxation parameter as in the previous section. For reference we perform a direct simulation with a dealiased Fourier scheme at a resolution of 4096 points, for which it was shown that the mesh-Reynolds number is on the order of unity [4].

In Fig. 10 the total energy $E(t) = 1/2 \int_{-\infty}^{+\infty} |\hat{u}(\xi)|^2 \, d\xi$ of the solution at times $t = 60$, 120, and 180 is compared with the direct simulation. The energy for the direct simulation was computed from the unfiltered solution. The model prediction agrees well with the direct simulation concerning energy magnitude and energy decay. The agreement improves with increasing resolution.

For illustration we show in Fig. 11 snapshots of the solutions at time $t = 180$. Instantaneous spectra at $t = 180$ clearly follow the theoretical ξ^{-2} drop-off and a good agreement with the direct simulation results is observed (Fig. 12).
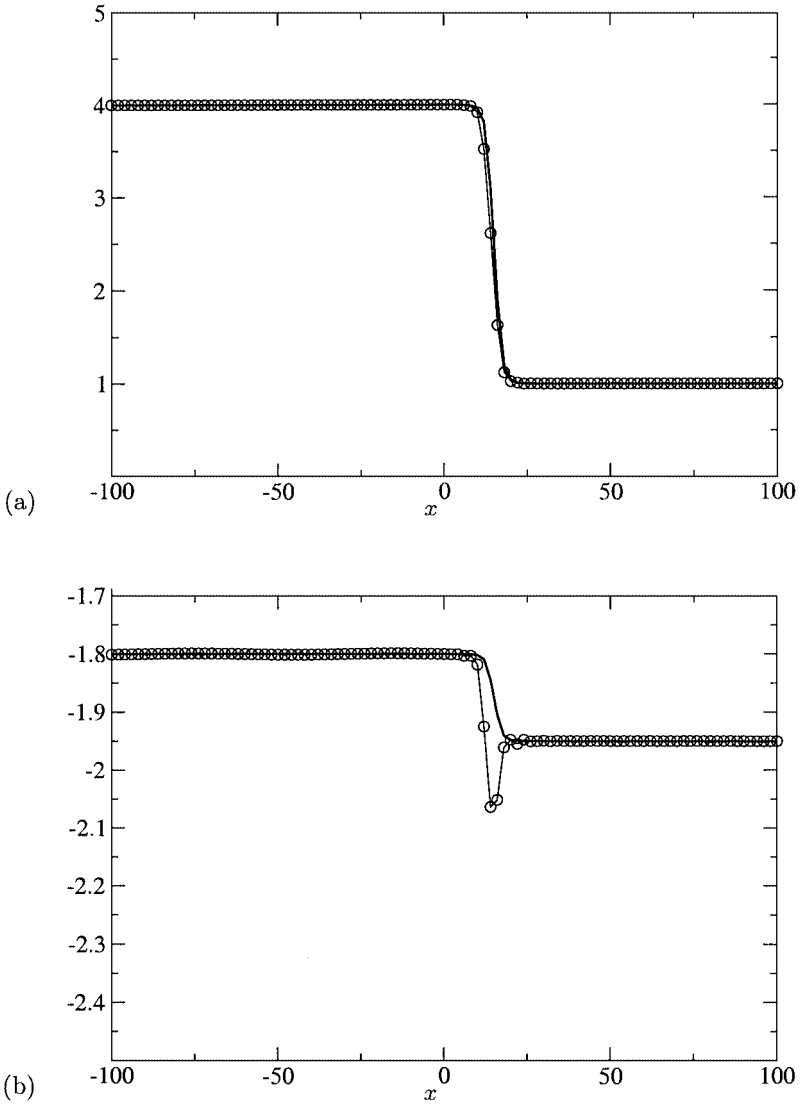
FIG. 13. Solution for the isothermal Euler equations (36) at $t = 300$, $N = 200$, $s = 0.05$, second-order secondary-filter $G_{2,1}$, $\chi = 1/2 + 60/h$. (a) Density: O–O–O, $\bar{\rho}$; ———, $\bar{\rho}_{exact}$. (b) Momentum: O–O–O, $\bar{m}$; ———, $\bar{m}_{exact}$.

5.3. Isothermal Euler Equations

The favorable resolution properties of the model which were observed in Section 5.1 let the method appear suitable for an application to the so-called "slow-shock problem" [39]. One considers the isothermal Euler equations given by (1) with

$$u = \begin{bmatrix} \rho \\ m \end{bmatrix} \quad \text{and} \quad F(u) = \begin{bmatrix} m \\ m^2/\rho + C_s^2 \rho \end{bmatrix}, \tag{36}$$

where ρ is the density, $m = \rho U$ the momentum, U the velocity, and C_s the constant speed of sound. In the following examples we set $C_s = 1$. The computational domain $-100 \leq$
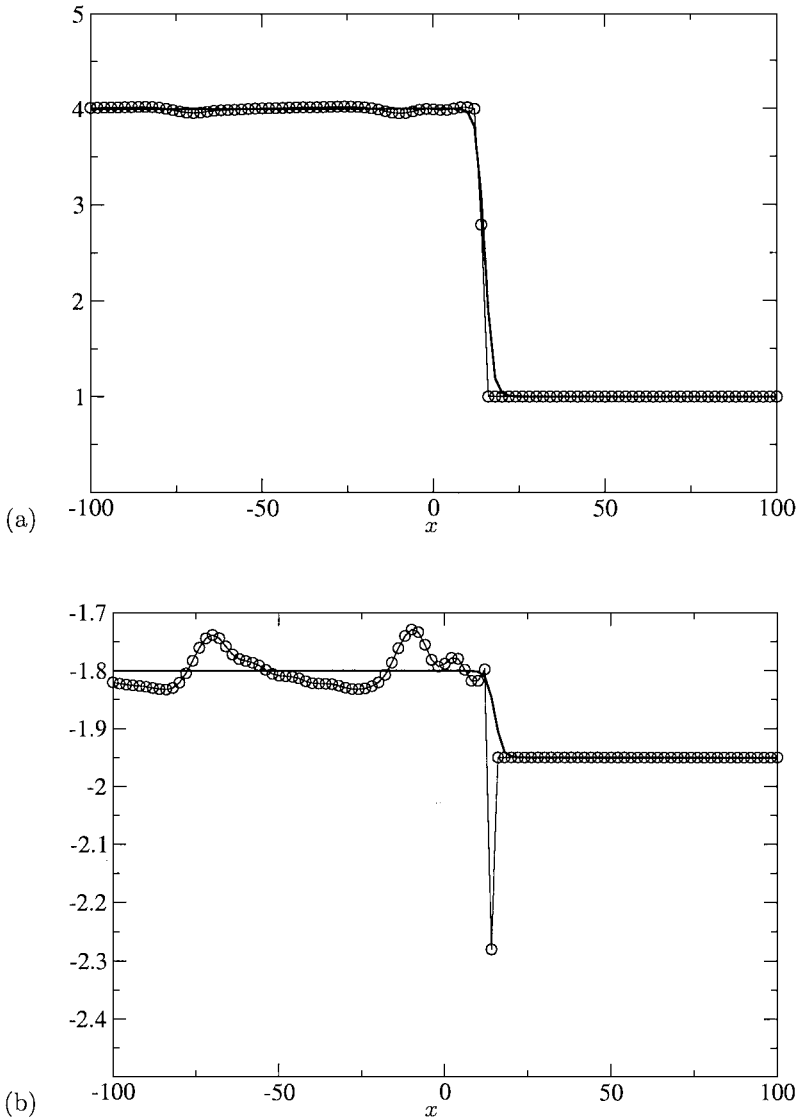
FIG. 14. Solution for the isothermal Euler equations (36) at $t = 300$, $N = 200$, and $s = 0.05$, third-order ENO scheme. (a) Density: O–O–O, ρ; ———, $\bar{\rho}_{exact}$. (b) Momentum: O–O–O, m; ———, $\bar{m}_{exact}$.

$x \leq 300$ is discretized by 200 subintervals, and the time step is determined by Eq. (35) with CFL $= 0.5$. Equation (1) with (36) has a traveling-wave solution

$$\rho = \begin{cases} 4 & \text{if } x < St, \\ 1 & \text{else,} \end{cases} \quad \text{and} \quad U = \begin{cases} S - 0.5 & \text{if } x < St, \\ S - 2 & \text{else,} \end{cases} \tag{37}$$

where U is the velocity and S is a given shock speed. Here we choose $S = 0.05$; i.e., the shock moves with 5% of the speed of sound.

Jin and Liu [21] have shown that for any smooth approximation of the shock wave the momentum profile necessarily develops a spike. For standard schemes such as the Lax–Friedrichs scheme and a first-order upwind scheme Karni and Čanić [23] show that the error in the momentum distribution can be as large as 300%.
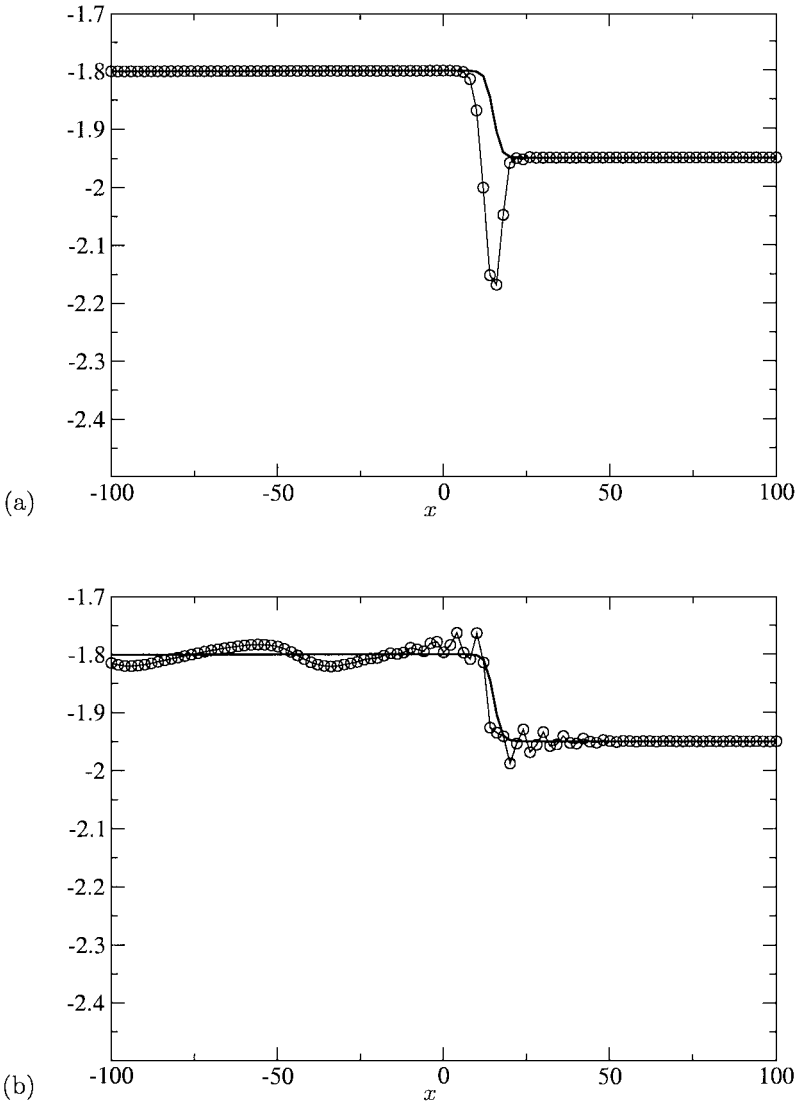
FIG. 15. Momentum distribution for the isothermal Euler equations (36) at $t = 300$, $N = 200$, and $s = 0.05$, with $\chi = 1 + 120/h$. O–O–O, $\bar{\rho}$; ——, $\bar{\rho}_{exact}$. (a) Second-order secondary filter $G_{2,1}$; (b) 12th-order secondary filter $G_{2,6}$.

For our computations, boundary conditions were imposed by specifying incoming Riemann variables in terms of the outgoing ones. For both primary and secondary filters no filtering is applied at the domain boundaries. We choose the relaxation parameter

$$\chi = \frac{1}{2} + \frac{60}{h}. \tag{38}$$

One could apply an estimate for χ similar to that given by Eq. (31) for the system of Eq. (36). Since the initial condition contains a filtered shock, whose gradient depends on the filter width, which again is related to the mesh width h, the first term on the right-hand side of Eq. (31) contains a factor $1/h$ as well. Given the above initial condition one can derive an estimate $\chi \simeq 600/h$, which was found to be too dissipative.
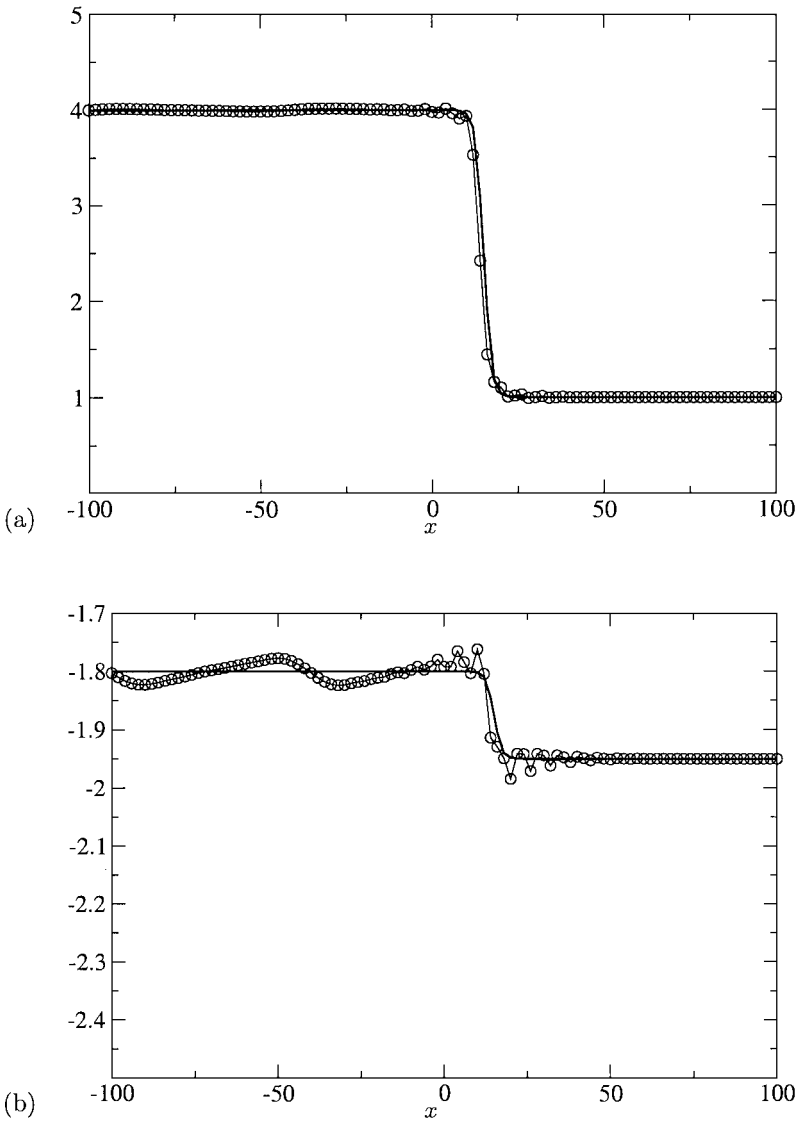
FIG. 16. Solution for the isothermal Euler equations (36) at $t = 300, N = 200, s = 0.05$, 12th-order secondary filter $G_{2,6}$, $\chi = 1/2 + 60/h$. (a) Density: O–O–O, $\bar{\rho}$; ———, $\bar{\rho}_{exact}$. (b) Momentum: O–O–O, $\bar{m}$; ———, $\bar{m}_{exact}$.

Figure 13 shows the results for the second-order secondary filter, obtained at $t = 300$, employing the same axis scaling as in [23]. We note that the expected spike in the momentum distribution has developed but is considerably smaller than with standard or high-resolution shock capturing schemes. For comparison we show in Fig. 14 results from a third-order essentially nonoscillatory scheme (ENO) employing a Roe-flux formulation [42]. Note also that for stable computation with the ENO scheme a characteristic flux decomposition was needed.

The absolute errors for our results with the DDM model are of the same magnitude for the density and the momentum distribution. Since due to the slow shock speed the momentum jump is much smaller than the density jump across the shock, the relative error in the momentum distribution is larger. The sensitivity to a different choice of χ is rather weak
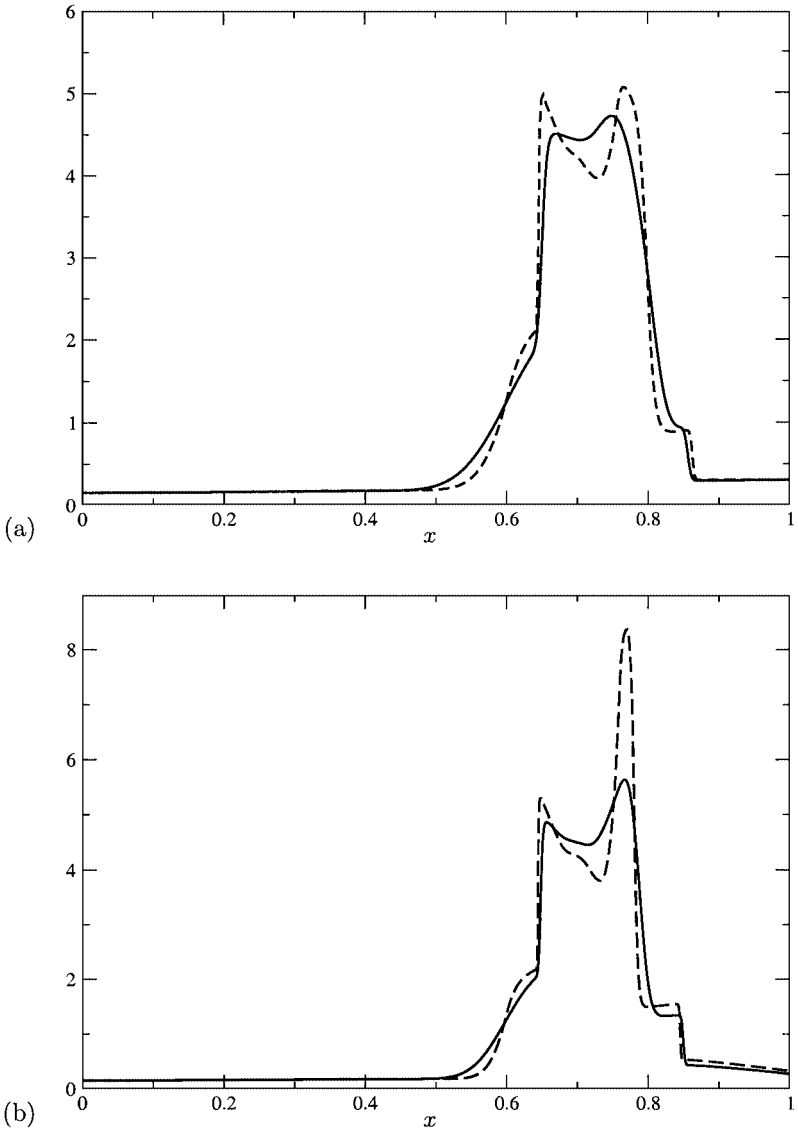
FIG. 17. Density distribution ρ for the blast-wave problem $t = 0.38$; $\chi = 1500/h$. ———, DDM with $G_{2,1}$; $----$, third-order ENO scheme. (a) $N = 400$; (b) $N = 800$.

(Fig. 15). A twice larger χ increases the error in the momentum distribution, which remains, however, smaller than for the ENO scheme (Fig. 14b). The 12th-order secondary filter $G_{2,6}$ fails to remove spurious oscillations from the solution (Figs. 15b and 16). Different choices for χ did not remedy this behavior.

5.4. Full Euler Equations

For the Euler equations u and $F(u)$ in Eq. (1) are given by

$$u = \begin{bmatrix} \rho \\ m \\ E \end{bmatrix} \quad \text{and} \quad F(u) = \begin{bmatrix} m \\ m^2/\rho + p \\ m(E + p)/\rho \end{bmatrix}, \tag{39}$$
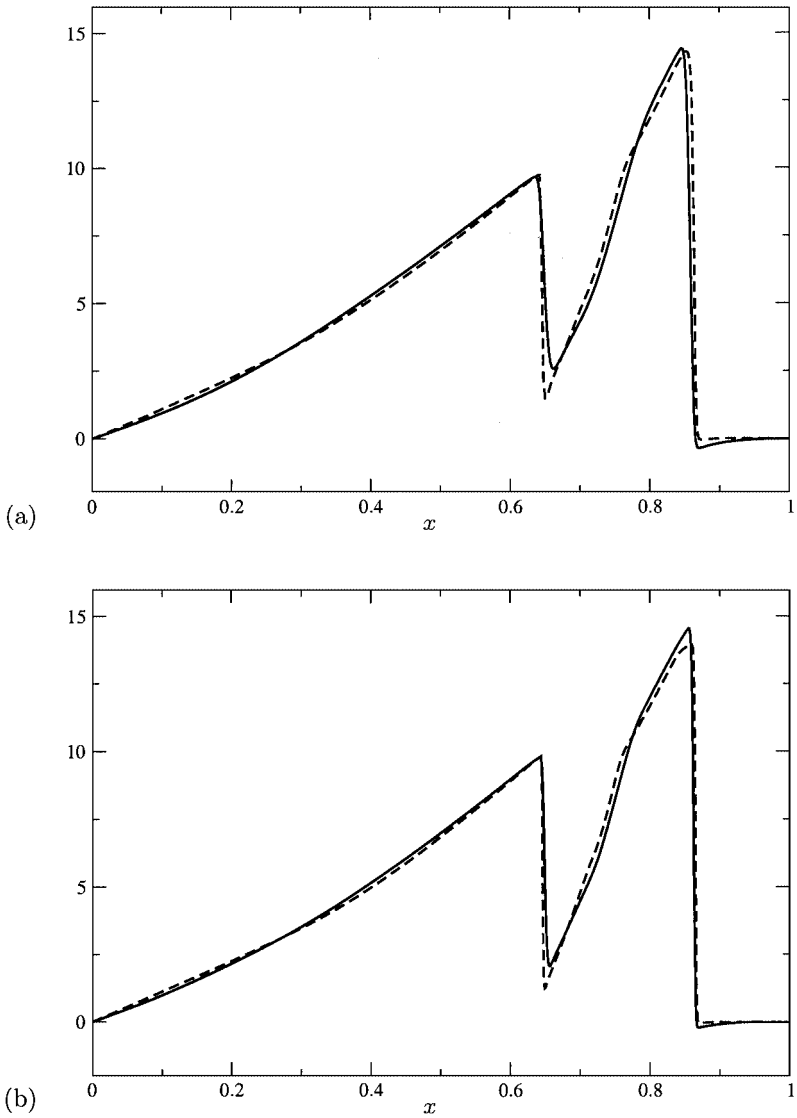
FIG. 18. Velocity distribution u for the blast-wave problem $t = 0.38$, $\chi = 1500/h$. ———, DDM with $G_{2,1}$; ————, third-order ENO scheme. (a) $N = 400$; (b) $N = 800$.

where $(x, t) \in [0, \infty) \times [x_0, x_1]$, $E = p/(\gamma - 1) + m^2/(2\rho)$ is the total energy, and p is the pressure.

5.4.1. Woodward–Colella Blast Wave

This configuration is a particularly challenging test for shock-capturing schemes, since it involves multiple interactions of shocks and rarefactions with each other and reflections from the solid walls at the domain boundaries. A detailed description and analysis of this test with several now classical shock-capturing schemes is given by Woodward and Colella [56]. The flow is described by the Euler equations (39) on the domain $(x, t) \in [0, \infty) \times [0, 1]$.
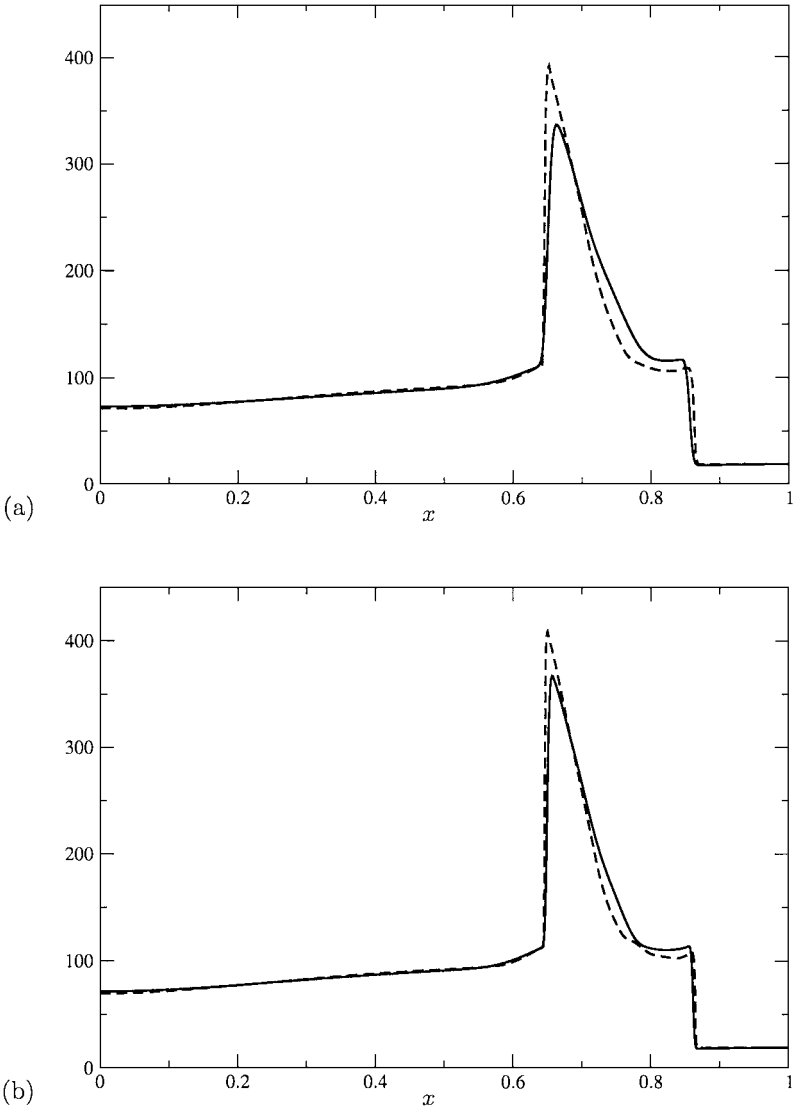
FIG. 19. Pressure distribution u for the blast-wave problem $t = 0.38$, $\chi = 1500/h$. ———, DDM with $G_{2,1}$; ----, third-order ENO scheme. (a) $N = 400$; (b) $N = 800$.

The initial condition is

$$u(0, x) = \begin{cases} \begin{bmatrix} 1 \\ 0 \\ 1000/(\gamma - 1) \end{bmatrix} & \text{if } 0 \leq x \leq 0.1, \\ \begin{bmatrix} 1 \\ 0 \\ 0.01/(\gamma - 1) \end{bmatrix} & \text{if } 0.1 \leq x \leq 0.9, \\ \begin{bmatrix} 1 \\ 0 \\ 100/(\gamma - 1) \end{bmatrix} & \text{if } 0.9 \leq x \leq 1, \end{cases} \tag{40}$$

where γ is set to 1.4. Boundary conditions at $x_0 = 0$ and $x_1 = 1$ are $u(x_0) = u(x_1) = 0$.
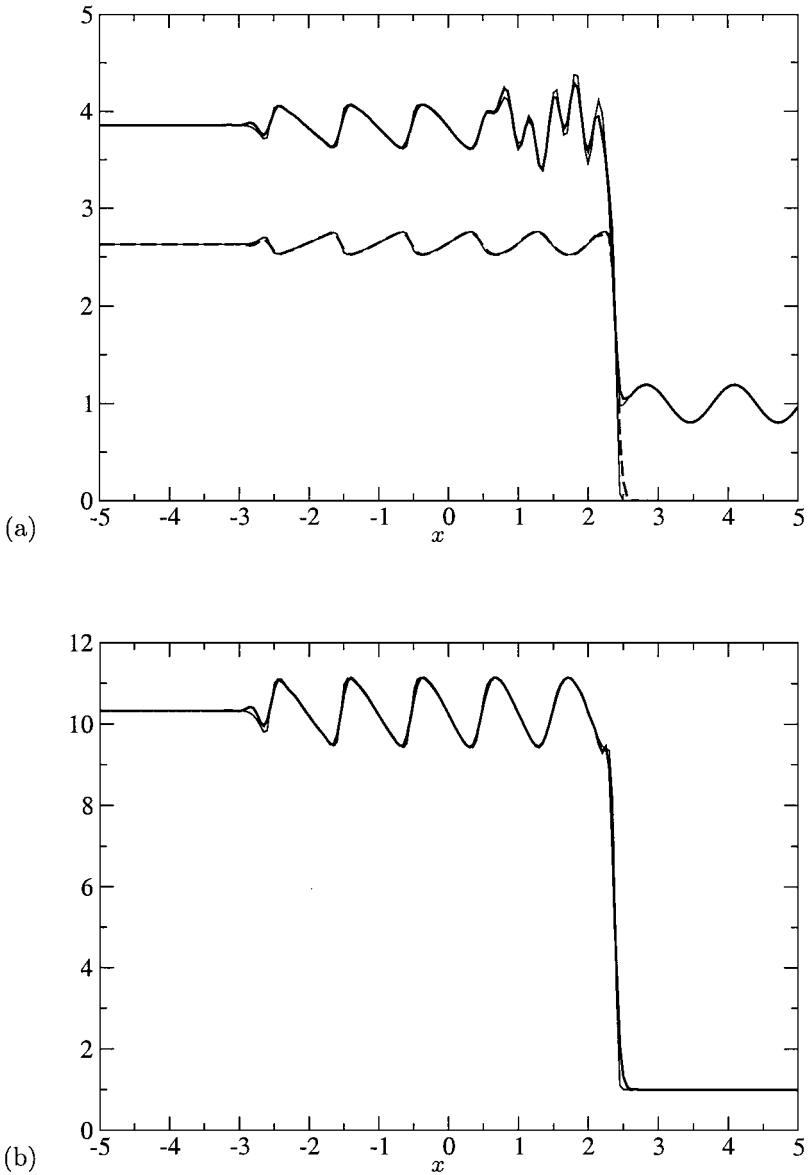
FIG. 20. Solution for the Euler equations (39) at $t = 1.8$, $N = 200$, second-order secondary filter $G_{2,1}$, $\chi = 1/2 + 60/h$. (a) Top down: ———, density $\bar{\rho}$; ————, velocity $\bar{u}$. (b) ———, Pressure $\bar{p}$; ———, filtered fifth-order ENO solution.

Computations are performed with the second-order secondary filter $G_{2,1}$. The relaxation parameter was set to $\chi = 1500/h$. Despite some experimentation with the relaxation parameter χ, for the 12th-order filter $G_{2,6}$ the computations terminated due to negative density when the most complex interaction at about $t = 0.029$ was reached (refer to Fig. 1 of Woodward and Colella [56]). Reference results were obtained with a third-order ENO scheme, as in the previous section. Results at $t = 0.38$ with $N = 400$ and 800 are shown in Figs. 17–19. The overall agreement is good, although for the DDM approach discontinuities are more smeared than with the ENO scheme.

5.4.2. *Shu–Osher Shock-Disturbance Interaction*

The full one-dimensional Euler equations with suitable initial conditions are used as a test problem for shock-turbulence interaction following the suggestion of Shu and Osher [42]. A $M = 3$ shock is moving into a density (or entropy) fluctuation field. The flow is governed by the Euler equations (39) for the domain $(x, t) \in [0, \infty) \times [-5, 5]$. For the numerical discretization the domain is partitioned into 200 subintervals. We impose an initial
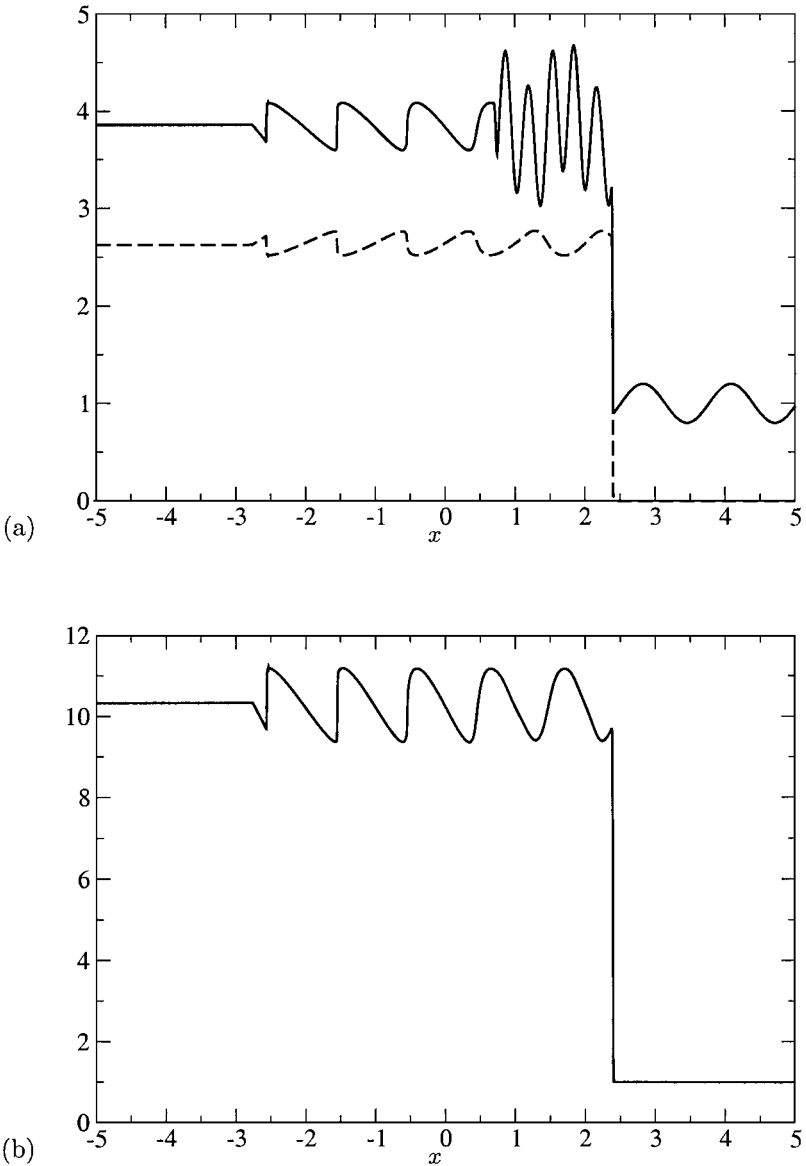

(a)

(b)

FIG. 21. Solution for the Euler equations (39) at $t = 1.8$, $N = 1600$, fifth-order ENO scheme. (a) Top down: ———, density ρ; – – – –, velocity u. (b) ———, Pressure p.
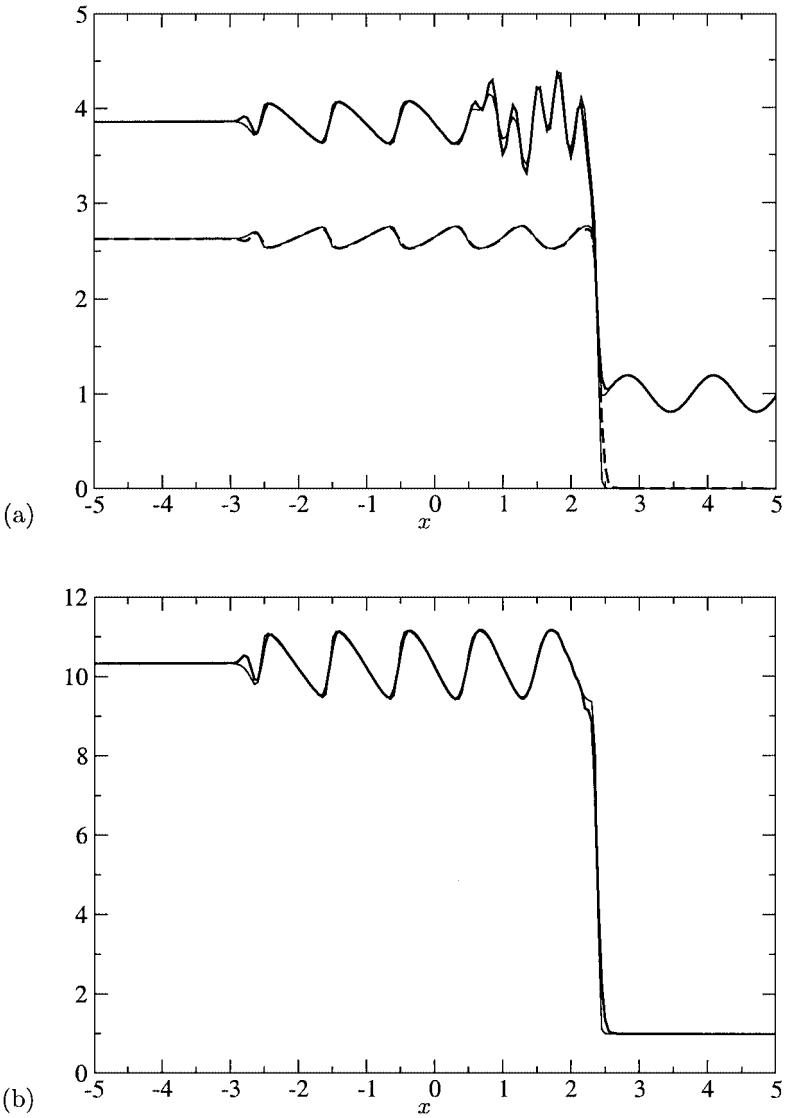
FIG. 22. Solution for the Euler equations (39) at $t = 1.8$, $N = 200$, 12th-order secondary filter $G_{2,6}$, $\chi = 1/2 + 60/h$. (a) Top down: ———, density $\bar{\rho}$; – – – –, velocity $\bar{u}$. (b) ———, Pressure $\bar{p}$; ———, filtered fifth-order ENO solution.

condition in accordance with Shu and Osher [42] as

$$
u(0, x) = \begin{cases} \begin{bmatrix} 3.857143 \\ 2.629369\, u_1(0, x) \\ \frac{31/3}{\gamma - 1} + \frac{1}{2} \frac{u_2(0,x)^2}{u_1(0,x)} \end{bmatrix} & \text{if } x < -4, \\[3em] \begin{bmatrix} 1 + 0.2 \sin 5x \\ 0 \\ 1/(\gamma - 1) \end{bmatrix} & \text{if } x \geq -4, \end{cases}
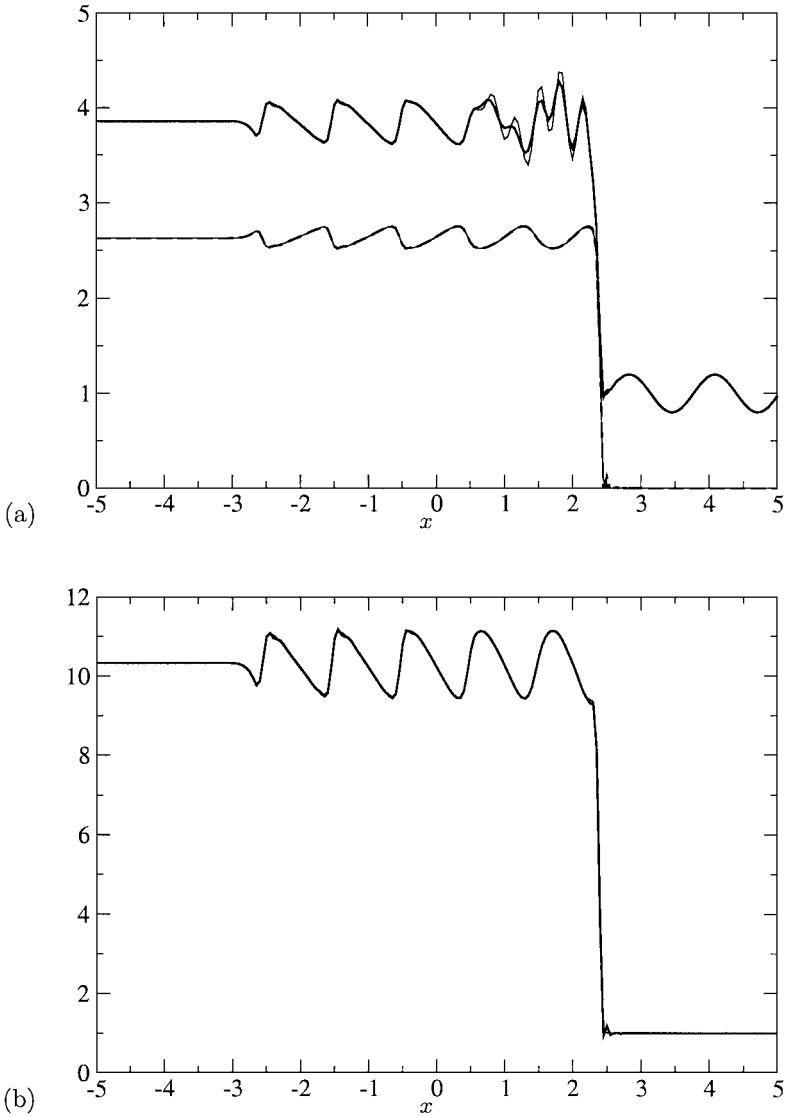\tag{41}
$$

where γ is set to 1.4.

FIG. 23. Solution for the Euler equations (39) at $t = 1.8$, $N = 200$, third-order ENO scheme. (a) Top down: ———, density ρ; – – – –, velocity u; (b) ———, Pressure p; ———, filtered fifth-order ENO solution.

We compare results obtained with DDM and a secondary filter of second-order and of twelfth-order with filtered data computed with a fifth-order ENO scheme using a Roe-flux formulation with entropy fix [42]. The relaxation parameter χ is set, as for the isothermal Euler equations in the previous section, by Eq. (38). For the initial conditions (41), at $t = 1.8$ (the time at which the numerical results are shown) the shock should have moved from $x = -4$ to 2.39, which coincides with the numerical results. The data for the second-order filter with Eq. (38) compare well with filtered fifth-order ENO data (Fig. 20). For reference, data computed with a fifth-order ENO scheme with $N = 1600$, for which grid convergence has been achieved, are shown in Fig. 21.

The 12th-order secondary filter gives similar results but is less dissipative on the large wavenumbers, and a small decompression shock develops at the trailing edge of the wave-train behind the shock (Fig. 22).
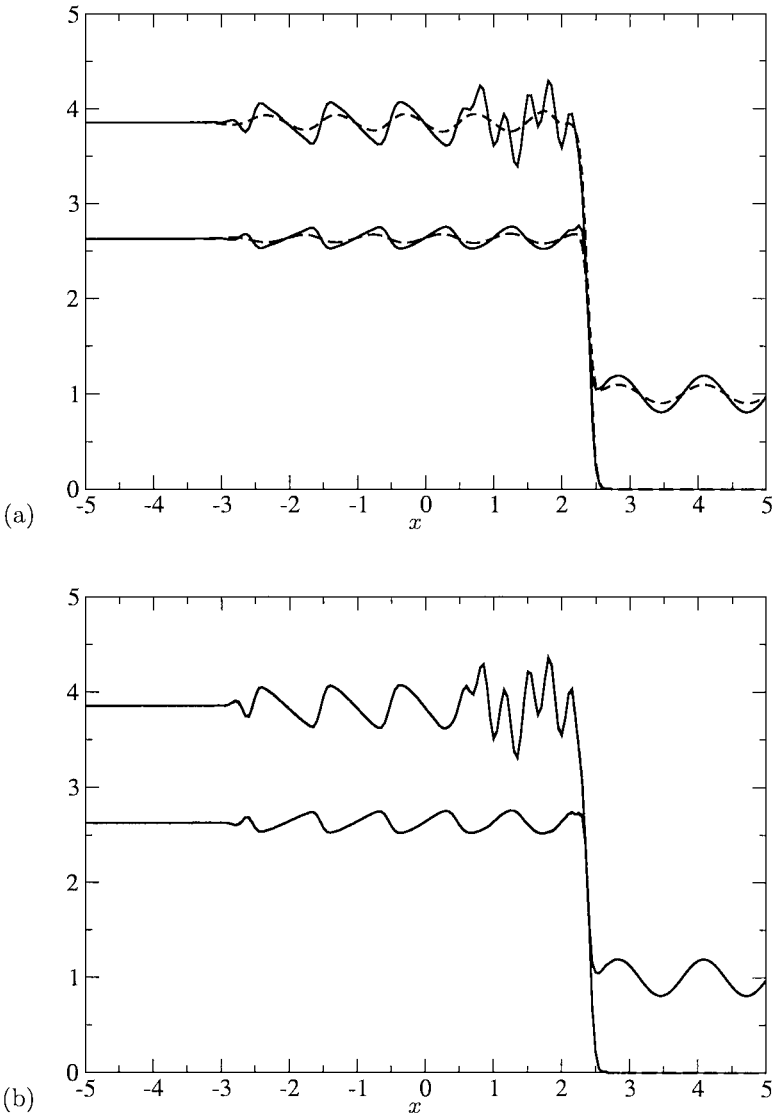
FIG. 24. Solution for the Euler equations (39) at $t = 1.8$, $N = 200$; ———, $\chi = 1/2 + 60/h$; $----$, $\chi = 1 + 120/h$. Top down: ———, density $\bar{\rho}$; $----$, velocity $\bar{u}$. (a) second-order secondary filter $G_{2,1}$; (b) 12th-order secondary filter $G_{2,6}$.

A comparison of the results in Fig. 20 and 22 with results obtained with a third-order ENO scheme using a Roe-flux formulation with entropy fix shows that the DDM approach gives a more accurate solution (Fig. 23).

Finally we assess the effect of a variation of the relaxation parameter. For a parameter

$$\chi = 1 + \frac{120}{h},$$

the solution with the 12th-order filter is almost identical to that with the previous choice for χ (Fig. 24b). With the second-order filter this value for χ is more dissipative for the wave train in the wake of the shock, yet the shock representation is in good agreement with the filtered ENO data (Fig. 24a).

6. CONCLUSIONS

The explicit use of filtering and defiltering has considerably improved the prediction capabilities of subgrid-scale modeling in LES [3]. For shock capture, filtering is mostly based on nonlinear approaches [24, 57], where regularization is achieved by limiters or ENO-type stencil switching. The spectral viscosity method of Tadmor [50] allows for an accurate representation of discontinuous solutions with a linear algorithm, involving, however, a dual-space representation of the solution. Given a primary filter which provides a certain smoothness of the solution of a given conservation law, the objective of the present approach is to devise a regularization which ensures that the filtered solution remains well resolved during time advancement. This is also the objective of subgrid-scale modeling with LES. Our proposed real-space regularization resembles a spectral viscosity. We have demonstrated that an *a priori* estimate for a linear regularization is possible. Generally we find a good agreement with filtered shock solutions. Results are without spurious oscillations around discontinuities if the secondary filter $G_{2,1}$ is employed. For the higher-order secondary filter spurious oscillations around discontinuities are observed for some of the investigated examples. An increase in the relaxation parameter is not sufficient to remove these oscillations. Additional postprocessing filtering or adjusting of the primary filter was not applied since this is not within our objective described above. Also, further extensions of the present approach may include nonlinear limiters or filters. Since our approach shares a considerable degree of commonality with recent deconvolution models for subgrid-scale modeling for LES [45, 47, 48] we expect that it will prove useful for the LES of shock-turbulence interaction.

REFERENCES

1. N. A. Adams, The role of deconvolution and numerical discretization in subgrid-scale modeling, in *Direct- and Large-Eddy Simulation IV*, edited by B. J. Geurts, R. Friedrich, and O. Métais (Kluwer Academic, Dordrecht), p. 311.

2. N. A. Adams, The use of LES subgrid-scale models for shock-capturing, *Int. J. Numer. Methods Fluids*, in Press.

3. N. A. Adams and S. Stolz, Deconvolution methods for subgrid-scale approximation in large-eddy simulation, in *Modern Simulation Strategies for Turbulent Flow*, edited by B. Geurts (Edwards, Ann Arbor, MI, 2001), p. 21.

4. A. A. Aldama, *Filtering Techniques for Turbulent Flow Simulation*, Lecture Notes in Engineering (Springer-verlag, New York, 1990), Vol. 56.

5. J. Bardina, J. H. Ferziger, and W. C. Reynolds, *Improved Turbulence Models Based on Large Eddy Simulation of Homogeneous, Incompressible, Turbulent Flows*. Technical Report TF-19 (Dept. of Mechanical Engineering, Stanford University, Stanford, CA, 1983).

6. J. P. Boris, F. F. Grinstein, E. S. Oran, and R. L. Kolbe, New insights into large eddy simulation, in *Fluid Dynamics Research* (North Holland, Amsterdam, 1992), Vol. 10, p. 199.

7. J. P. Boyd, Two comments on filtering (artificial viscosity) for Chebyshev and Legendre spectral and spectral element methods: preserving boundary conditions and interpretation of the filter as diffusion, *J. Comp. Phys.* **143**, 283 (1998).

8. J. W. Deardorff, A numerical study of three-dimensional turbulent channel flow at large Reynolds number, *J. Fluid Mech.* **41**, 453 (1970).

9. J. A. Domaradzki and N. A. Adams, Modeling subgrid scales of turbulence in large-eddy simulations, *J. Turb.*, in press.

10. G. L. Eyink, Energy dissipation without viscosity in ideal hydrodynamics. I. Fourier analysis and local energy transfer, *Phys. D* **78**, 222 (1994).

11. C. Fureby and F. F. Grinstein, Monotonically integrated large eddy simulation of free shear flows, *AIAA J.* **37**, 544 (1999).

12. E. Garnier, M. Mossi, P. Sagaut, P. Comte, and M. Deville, On the use of shock-capturing schemes for large-eddy simulation, *J. Comput. Phys.* **153**, 273 (1999).

13. M. Germano, U. Piomelli, P. Moin, and W. H. Cabot, A dynamic subgrid-scale eddy viscosity model, *Phys. Fluids A* **3**, 1760 (1991).

14. B. Gustafsson, H.-O. Kreiss, and J. Oliger, *Time Dependent Problems and Difference Methods* (Wiley, New York, 1995).

15. E. J. Gutmark and F. F. Grinstein, Flow control with noncircular jets, *Annu. Rev. Fluid Mech.* **31**, 239 (1999).

16. A. Harten, B. Engquist, S. Osher, and S. Chakravarthy, Uniformly high order essentially non-oscillatory schemes, III, *J. Comp. Phys.* **71**, 231 (1987).

17. T. J. R. Hughes and A. Brooks, A multidimensional upwind scheme with no crosswind diffusion, in *Finite Element Methods for Convection Dominated Flows*, edited by T. J. R. Hughes (ASME, Fairfield, 1979), p. 19.

18. T. J. R. Hughes, M. Mallet, and A. Mizukami, A new finite-element formulation for computational fluid dynamics. II: Beyond SUPG, *Comput. Methods Appl. Mech. Eng.* **54**, 341 (1986).

19. J. Jiménez, Limits and performance of eddy viscosity sub-grid models, in *Direct and Large-Eddy Simulation III*, edited by P. Voke, N. D. Sandham, and L. Kleiser (Kluwer Academic, Dordrecht/Norwell, MA, 1999), p. 75.

20. J. Jiménez and R. D. Moser, Large-eddy simulations: Where are we and what can we expect, *AIAA J.* **38**, 605 (2000).

21. S. Jin and J.-G. Liu, The effects of numerical viscosities. I. Slowly moving shocks. *J. Comp. Phys.* **126**, 373 (1996).

22. G.-S. Karamanos and G. E. Karniadakis, A spectral vanishing viscosity method for large-eddy simulations, *J. Comput. Phys.* **163**, 22 (2000).

23. S. Karni and S. Čanić, Computations of slowly moving shocks, *J. Comp. Phys.* **136**, 132 (1997).

24. F. Lafon and S. Osher, High order filtering methods for approximating hyperbolic systems of conservation laws, *J. Comp. Phys.* **96**, 110 (1991).

25. P. D. Lax, *Hyperbolic Systems of Conservation Laws and the Mathematical Theory of Shock Waves* (SIAM-CBMS, Philadelphia, 1973).

26. P. D. Lax and B. Wendroff, Systems of conservation laws, *Commun. Pure Appl. Math.* **13**, 217 (1960).

27. S. K. Lele, Compact finite difference schemes with spectral-like resolution, *J. Comp. Phys.* **103**, 16 (1992).

28. A. Leonard, Energy cascade in large eddy simulations of turbulent fluid flows, *Adv. Geophys.* **18A**, 237 (1974).

29. A. Leonard and G. Winckelmans, A tensor-diffusivity sub-grid model for large-eddy simulation, in *Direct and Large-Eddy Simulation III*, edited by P. Voke, N. D. Sandham, and L. Kleiser (Kluwer Academic, Dordrecht/Norwell, CA, 1999), p. 147.

30. M. Lesieur, *Turbulence in Fluids* (Kluwer Academic, Dordrecht/Norwell, MA, 1997), 3rd ed.

31. M. Lesieur and O. Métais, New trends in large-eddy simulations of turbulence. *Annu. Rev. Fluid. Mech.* **28**, 45 (1996).

32. Y. Maday, S. M. Ould Kaber, and E. Tadmor, Legendre pseudospectral viscosity method for nonlinear conservation laws, *SIAM J. Numer. Anal.* **30**, 321 (1993).

33. L. G. Margolin and W. J. Rider, A rationale for implicit turbulence modeling, in *CD Proceedings of the ECCOMAS CFD 2001 Conference, Swansea* (IMA, Essex, 2001).

34. Ch. Meneveau and J. Katz, Scale-invariance and turbulence models for large-eddy simulation, *Annu. Rev. Fluid. Mech.* **32**, 1 (2000).

35. O. Métais and M. Lesieur, Spectral large-eddy simulations of isotropic and stably-stratified turbulence, *J. Fluid Mech.* **239**, 157 (1992).

36. D. H. Porter, P. R. Woodward, and A. Pouquet, Inertial range structures in decaying compressible turbulent flows, *Phys. Fluids* **10**, 237 (1998).

37. C. D. Pruett and N. A. Adams, A priori analyses of three subgrid-scale models for one-parameter families of filters, *Phys. Fluids* **12**, 1133 (2000).

38. R. D. Richtmyer and K. W. Morton, *Difference Methods for Initial-Value Problems* (Wiley, New York, 1965), 2nd ed.

39. Th. W. Roberts, The behavior of flux difference splitting schemes near slowly moving shock waves, *J. Comp. Phys.* **90**, 141 (1990).

40. Ph. Rosenau, Extending hydrodynamics via the regularization of the Chapman–Enskog expansion, *Phys. Rev. A* **40**, 7193 (1989).

41. S. Schochet and E. Tadmor, The regularized Chapman–Enskog expansion for scalar conservation laws, *Arch. Rat. Mech. Anal.* **119**, 95 (1992).

42. C.-W. Shu and S. Osher, Efficient implementation of essentially non-oscillatory shock-capturing schemes, II, *J. Comput. Phys.* **83**, 32 (1989).

43. J. Smagorinsky, General circulation experiments with the primitive equations, *Mon. Weather Rev.* **93**, 99 (1963).

44. J. Smagorinsky, Some historical remarks on the use of nonlinear viscosities, in *Large Eddy Simulation of Complex Engineering and Geophysical Flows*, edited by B. Galperin and S. A. Orszag (Cambridge University Press, Cambridge, UK, 1993), p. 3.

45. S. Stolz and N. A. Adams, An approximate deconvolution procedure for large-eddy simulation, *Phys. Fluids* **11**, 1699 (1999).

46. S. Stolz, N. A. Adams, and L. Kleiser, The approximate deconvolution model for compressible flows: isotropic turbulence and shock-boundary-layer interaction, in *Advances in LES of Complex Flows* edited by R. Friedrich and W. Rodi (Kluwer Academic, Dordrecht/Norwell, CA, 2002).

47. S. Stolz, N. A. Adams, and L. Kleiser, An approximate deconvolution model for large-eddy simulation with application to incompressible wall-bounded flows, *Phys. Fluid* **13**, 997 (2001).

48. S. Stolz, N. A. Adams, and L. Kleiser, The approximate deconvolution model for LES of compressible flows and its application to shock-turbulent-boundary-layer interaction, *Phys. Fluids* **13**, 2985 (2001).

49. I. V. Sytine, D. H. Porter, P. R. Woodward, S. W. Hodson, and K.-H. Winkler, Convergence tests for the piece-wise parabolic method and Navier-Stokes solutions for homogeneous compressible turbulence, *J. Comput. Phys.* **158**, 225 (2000).

50. E. Tadmor, Convergence of spectral methods for nonlinear conservation laws, *SIAM J. Numer. Anal.* **26**, 30 (1989).

51. E. Tadmor, Shock capturing by the spectral viscosity method, *Comp. Methods Appl. Mech. Eng.* **80**, 197 (1990).

52. E. Tadmor, Super-viscosity and spectral approximations of nonlinear conservation laws, in *Numerical Methods for Fluid Dynamics*, edited by M. J. Baines and K. W. Morton (Clarendon, Oxford, 1993), Vol. 4, p. 69.

53. E. F. Toro, *Riemann Solvers and Numerical Methods for Fluid Dynamics: A Practical Introduction* (Springer-Verlag, Berlin, 1999), 2nd ed.

54. R. Vichnevetsky and J. B. Bowles, *Fourier Analysis of Numerical Approximations of Hyperbolic Equations* (SIAM, Philadelphia, PA, 1982).

55. J. H. Williamson, Low-storage Runge–Kutta schemes. *J. Comput. Phys.* **35**, 48 (1980).

56. P. Woodward and P. Colella, The numerical simulation of two-dimensional flow with strong shocks, *J. Comp. Phys.* **54**, 115 (1984).

57. H. C. Yee, N. D. Sandham, and M. J. Djomehri, Low-dissipative high-order shock-capturing methods using characteristic-based filters, *J. Comp. Phys.* **150**, 199 (1999).